Platelets favor the outgrowth of established metastases

Maria J. Garcia-Leon[1-4], Olivier Lefebvre[1-4], Gautier Follain[1-4,7], Clarisse Mouriaux[5], Ignacio Busnelli[1-4], Annabel Larnicol[1-4,6], Florent Colin[1-4], Vincent Mittelheisser[1-4], Marina Peralta[1-4], Catherine Bourdon[5], Raphael Samaniego[1-3], Pierre H. Mangin[5,✉], and Jacky G. Goetz[1-4,✉]

[1]Tumor Biomechanics, INSERM UMR-S1109, Strasbourg, F-67000, France.
[2]Université de Strasbourg, Strasbourg, F-67000, France.
[3]Fédération de Médecine Translationnelle de Strasbourg (FMTS), Strasbourg, F-67000, France.
[4]Equipe Labellisée Ligue Contre le Cancer.
[5]UMR-S1255, INSERM, Etablissement Français du Sang-Alsace, Université de Strasbourg, F-67000, France.
[6]Instituto de Investigación Sanitaria Gregorio Marañón (IISGM), Unidad de Microscopía Confocal, Madrid, Spain.
[7]Present address: Turku Bioscience Centre, University of Turku and Åbo Akademi University, Turku, Finland

Despite abundant evidence demonstrating that platelets foster metastasis, a therapeutic approach based on anti-platelet agents is not an option due to the risk of hemorrhages. In addition, whether platelets can regulate metastasis at the late stages of the disease remains unknown. In this study, we subjected syngeneic models of metastasis to various thrombocytopenic regimes to show that platelets provide a biphasic contribution to metastasis. While potent intravascular binding of platelets to tumor cells efficiently promotes metastasis, platelets further support the outgrowth of established metastases. Genetic depletion and pharmacological targeting of the platelet-specific receptor GPVI in humanized mouse models efficiently reduced the growth of established metastases, independently of active platelet binding to tumor cells in the bloodstream. Our study is the first to demonstrate therapeutic efficacy when targeting animals carrying growing metastases. It further identifies GPVI as the first molecular target whose inhibition can impair metastasis without inducing collateral hemostatic perturbations.

Keywords: Platelets, metastasis, binding, aggregation, targeted therapy

Correspondence: ***jacky.goetz@inserm.fr (www.goetzlab.fr ; @GoetzJacky) and pierre.mangin@efs.sante.fr***

DRAFT

INTRODUCTION

Metastasis is a pathological process during which tumor cells (TCs) detach from the primary tumor, intravasate into the blood or lymphatic circulation, and colonize distant organs. One of the most frequent target organs of metastatic cancers is the lungs (Valastyan Weinberg, 2011). Around 21–32% of breast cancers are accompanied by lung metastases (Wu et al., 2017), which dramatically impacts patient mortality (Schlappack, Baur, Steger, Dittrich, Moser, 1988). Yet, the fundamental mechanisms driving lung metastasis remain poorly understood. While circulating tumor cells (CTCs) face several hostile forces in the bloodstream that are detrimental to their survival (Follain et al., 2020), they can exploit them to arrest and successfully grow upon extravasation (Follain et al., 2018; Osmani et al., 2019; Osmani et al., 2021). In addition, CTCs further exploit the bloodstream ecosystem and interact as clusters or with blood components on their way to metastasis (Aceto et al., 2014; Gkountela et al., 2019; Peralta, Osmani, Goetz, 2022; Szczerba et al., 2019).

Among these, platelets are major allies and promote the metastatic progression of cancers (Labelle, Begum, Hynes, 2014). Platelets can protect TCs from destruction by shear forces, favor adhesion and extravasation at distant sites, favor immune evasion, mediate a tumor-prone inflammation, or favor neo-angiogenesis (Haemmerle, Stone, Menter, Afshar-Kharghan, Sood, 2018). While recent work suggests that platelets can control tumor initiation and growth, as shown recently in the liver (Ma et al., 2022; Senft, 2022) and are recruited to ovarian tumors by thrombopoietic cytokines to further fuel tumor growth (Stone et al., 2012), abundant research demonstrates that they mostly promote tumor cell metastasis. A seminal study documented the inhibition of metastasis by platelet depletion, which can be rescued by platelets transfusion (Gasic, Gasic, Stewart, 1968). The depletion of platelet receptors such as the vWF receptor GPIb, and the collagen receptor GVPI, results in the inhibition of lung metastasis of melanoma B16F10 and lung carcinoma D121 cells, respectively (Jain, Russell, Ware, 2009; Jain et al., 2007). CTCs rapidly bind, activate, and aggregate circulating platelets through the so-called Tumor Cell-Induced Platelet Aggregation (TCIPA). This provides a physical shield to CTCs and favors intravascular arrest and survival (Karreman et al., 2016; Labelle Hynes, 2012; Nieswandt, Hafner, Echtenacher, Mannel, 1999) as well as successful extravasation and metastatic outgrowth (Feinauer et al., 2020; Schumacher, Strilic, Sivaraj, Wettschureck, Offermanns, 2013). However, these studies mostly focus on early and intravascular steps of metastasis that depend on platelet-tumor interactions. Furthermore, they assume that all cancers interact equivalently with platelets which altogether, from a clinical perspective, leaves a unique window of intervention: impairing platelet-tumor cell interaction in the bloodstream. Finally, such an assumption may lead to controversial results in different cancer models (Erpenbeck, Nieswandt, Schon, Pozgajova, Schon, 2010) (Echtler et al., 2017) and an unclear outcome when using anti-platelet drugs in oncologic patients (reviewed in (Lucotti Muschel, 2020)), issues that exclude these drugs from standard cancer treatments and/or prophylaxis.

Building on such limitations, we designed a study aiming at providing a comprehensive characterization of the efficiency of interaction between platelets and a panel of metastatic TC types. These models were then subjected to several throm-

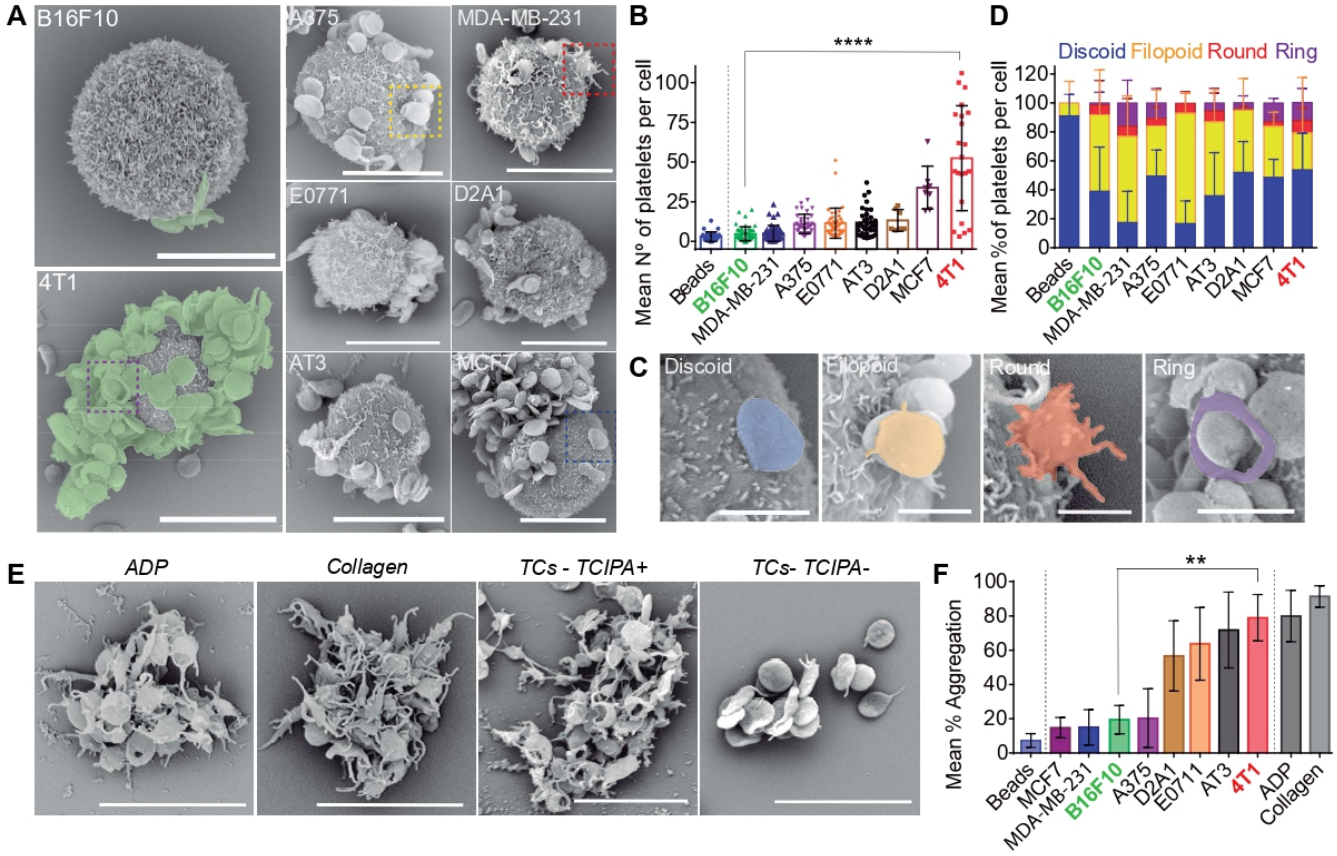

Fig. 1. TCs bind and aggregate blood platelets with different efficiencies (A) SEM images of TCs interacting with mouse platelets contained within mouse citrated platelet rich plasma (cPRP). Mouse breast carcinoma (4T1) and mouse melanoma (B16F10) cells are highlighted, as they show the most different platelet binding profiles (high versus low, respectively). (B) Platelet binding profiles quantification graph of (A). Kluskal-Wallis with False discovery rate post-test, mean +-SD. (C) SEM images details of TC-bound platelets at different activation states including: discoid (resting), filopoid (low activation) and round (full activation). Ring-shaped platelets of unknown function were also observed in a minor frequency. (D) Relative number (%) of each platelet shape per TC, activation stages are color-coded. Representative data from a total of 10 to 50 images per cell line from 2 to 4 independent experiments. (E) SEM images of human platelet aggregates obtained after the 30 minutes of platelet aggregation assay using human PRP with ADP and collagen as classic agonists, and TCs able to induce (TCIPA+) or not (TCIPA-) platelet aggregation. (F) Relative (%) mean platelet aggregation in tested TCs. Kluskal-Wallis with False discovery rate post-test, mean +-SD.

bocytopenic (TCP) regimes in mouse models to interrogate a putative late contribution of platelets to metastatic outgrowth, which could be targeted with new treatment strategies. We show that platelets bind TCs with different efficiencies and that is crucial for the adhesion and survival of TCs within the vasculature. Importantly, we provide evidence that platelet binding profiles scale with their long-term metastatic potential in vivo, and that platelets efficiently colonize mouse and human lung metastatic foci. Depletion of platelets in animals carrying growing metastases was sufficient to reduce metastatic outgrowth demonstrating, for the first time, that platelets favor metastasis independently of platelet-tumor cell interaction in the bloodstream. Genetic depletion and pharmacological targeting of the platelet-specific receptor GPVI in humanized mouse models efficiently reduced the growth of established metastases, independently of active platelet binding to tumor cells in the bloodstream. Our findings highlight, for the first time, that interfering with the collagen receptor GPVI can impair metastatic outgrowth of already established metastatic and addresses the most frequent scenario for therapeutic intervention in oncologic patients, namely the presence of a primary tumor with one or several metastatic sites.

RESULTS

Tumor cells bind and activate platelets in vitro with different efficiencies.

Platelets have been reported to bind circulating TCs (Labelle et al., 2014) but whether this applies to every cell type remains unknown. We first checked in vitro the efficiency of human platelets to interact with various human and mouse tumor cell lines, either from breast cancer (epithelium-derived) or melanoma, using scanning electron microscopy (SEM). We found out that platelets do not equally bind TCs (Fig.1A-B). While some cell lines such as 4T1 or MCF7 efficiently bind platelets, other cell lines such as B16F10 and MDA-MB-231 can't bind more platelets than passive beads (Fig. 1A-B, S1A). We assessed the morphology of bound platelets (Fig.1C-D) and carefully probed their activation through their ability to promote TCIPA (Fig.1E-F) which correlated with platelet binding, thus indicating that TCs behave as weak platelet agonists. We further observed that TCs efficiently bind platelets in the absence of plasma proteins (Fig.S1E-F) but fail to promote aggregation (Fig.S1B,D) or activate them (Fig.S1G-H). Altogether, these data indicate that TCs do not equally bind and activate platelets, raising the possi-

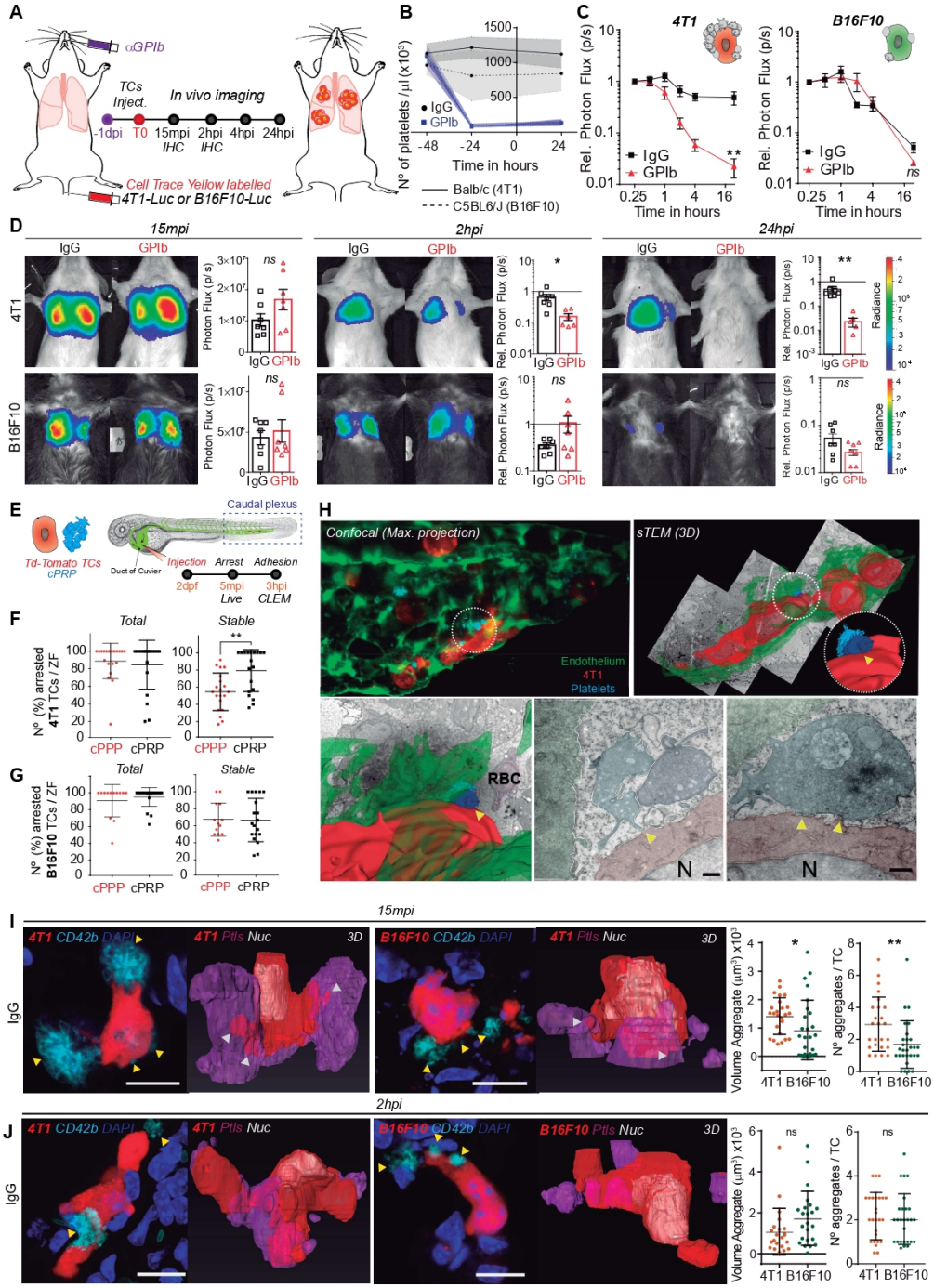

Fig. 2. In vivo lung seeding of 4T1 or B16F10 TCs is differentially influenced by platelets (A) Infographics showing the experimental setting to study the early steps (24h) of the metastatic cascade in mice in the presence or absence of platelets. Cell Trace-labelled 4T1-Luc or B16F10-Luc TCs are injected intravenously in normal or thrombocytopenic (TCP) mice (IgG- or GPIb-treated, respectively) 1 day post-treatment (1dpi). Lung seeding is followed by in vivo bioluminescence and analysis of arrested single cells is performed by immunohistochemistry at 15 minutes port-injection (15mpi) and 2 hours post-injection (2hpi). (B) Graph showing platelet counts on IgG- and GPIb-treated Balb/c and C5BL6/J animals. (C) Kinetics of 4T1-Luc and B16F10-Luc TCs lung seeding during 24 hours in normal and TCP mice, express as a ratio according to the initial 15mn signal input. Two-way Anova with false discovery rate post-test, mean +/-SEM, 2 independent experiments of n=3 to 4. (D) Representative images and time point comparisons of total lung bioluminescence in normal versus TCP animals in 4T1 (up) and B16F10 (down) TCs models. Data are represented as mean +/- SEM, Mann-Whitney analysis. (E) Infographics showing the experimental setting to study the early steps of the metastatic cascade in vivo in the ZF embryo. Td-tomato-expressing 4T1 or B16F10 cells are intravenously microinjected into the ZF embryo via the duct of Cuvier, together with human cPPP (control) or human cPRP. TCs circulation and arrest are imaged immediately (5mpi) by live video microscopy. Stable adhesion and TC-platelet interactions are imaged by confocal microscopy at 3hpi. (F) Quantification of total and stable arrest of 4T1 cells in the caudal plexus of the ZF embryo during 5 minutes of live video microscopy. Mann-Whitney test, mean +/- SD, 4 independent experiments with a minimum of 15 ZF embryos per experiment. (G) Quantification as in (F) for B16F10 cells. (H) Representative confocal and CLEM images of 4T1 cells arrested intravascularly in the caudal plexus of the ZF embryo after 3hpi. Arrowheads indicate contact between platelets and TCs. Asterisks indicate contact between platelets and endothelium. SEM scale: 500nm. 5 to 10 ZF were injected with 4T1 cells in 3 independent experiments; only one representative fish was selected for CLEM analysis. (I) Representative confocal images of single 4T1 or B16F10 cells arrested in control and TCP mouse lungs at 15mpi. Arrowheads show the interaction of single platelets and platelet aggregates with the TCs. Scale bars 10m. On the right, the volume and number of platelet aggregates around the arrested TCs in normal and TCP mice. Platelet and TCs volumes were calculated by TC and platelets segmentation in AMIRA. Mann-Whitney test, mean +/- SD, 1 independent experiment with 25 single-cell images per group. (J) Representative confocal images of single 4T1 or B16F10 cells arrested in normal and TCP mouse lungs at 2hpi. Arrowheads show the interaction of single platelets and platelet aggregates with the TCs. Scale bars 10m. On the right, the volume and number of platelet aggregates around the arrested TCs in normal and TCP mice. Same analysis as in (I)

bility that both processes directly impact the metastatic properties of TCs. To test such a hypothesis and further study how platelets shape metastasis, we selected two mouse tumor cell lines with opposite binding and platelet activation behavior (4T1 vs B16) that are compatible with experimental metastasis approaches in a syngeneic background (Balb/c and C57BL/6 respectively).

Platelets orchestrate the intravascular behavior of circulating TCs and control lung seeding in vivo.

It is well-established that the early seeding of TCs shapes their metastatic potential (Headley et al., 2016). We next interrogated whether differential platelet binding to TCs may influence metastasis in vivo. To do so, we designed an experimental lung metastasis assay that allows us to probe the behavior of TCs at very early and sequential steps of the metastatic cascade (Fig.2A). We depleted platelets using an α-GPIb treatment that proved to be equally and highly efficient in two animal models (Balb/c and C57BL/6, Fig.2B) and assessed TCs lung seeding by sequential in vivo imaging of 4T1 or B16F10 luciferase-expressing cells, starting from 15 minutes post-injection (mpi) up to 24 hours post-injection (hpi) (Fig.2A). High-bind 4T1 cells reached (15 mpi) and efficiently seeded the lungs (24 hpi) upon clearance from 0 to 24 hpi (33-fold), as shown previously (Headley et al. Nature 2016 + other refs). However, when 4T1 cells were injected in thrombocytopenic mice, lung seeding was drastically reduced by 10-fold when compared to control conditions. In contrast, the lung seeding potential of low-bind B16F10 cells was low when compared to 4T1 and, most importantly, independent of the presence of platelets (Fig.2C-D). These data suggest that lung seeding scales with the platelet binding potential of TCs can be perturbed by reducing platelet counts.

To provide a live and quantitative description of this platelet-dependent intravascular arrest of TCs, we next used our previously-established experimental metastasis model in the zebrafish embryo (Follain et al., 2018). Fluorescently-labeled TCs and human citrated platelet-rich plasma (cPRP) were co-injected in the duct of Cuvier of Tg(Fli1a:GFP) embryos at 2 days post-fertilization (dpf) and live-monitored during 5 minutes post-injection (mpi) (Fig.2E). Careful live tracking of TCs, as done previously (Follain et al., 2018), showed that platelets favor the stable arrest of 4T1 in the caudal plexus (Fig.2F, S2A) thus reducing their circulation time (Fig.S2A). In contrast, platelets did not affect the circulation and arrest patterns of B16F10 (Fig.2G, Fig.S2B). A heat mapping analysis that allows quantitatively locating the hotspot of the arrest of TCs revealed that platelets favored the stable arrest of 4T1 cells in high shear arterial vessels (DA, dorsal aorta; CV, caudal vein) without impacting the entry of TCs into small sized vessels (ISV, inter-somitic vessels, Fig.S2A,C,D) where TCs mostly arrest through physical constraint imposed by blood vessels. Interestingly, although they did not affect the number of stable arrest events occurring for B16F10 in non-constraining arterial vessels, platelets favored the entry and arrest into intersomitic vessels (Fig.S2B,C,D). We probed arrest events at the nanoscale using correlative light electron microscopy (CLEM) (Follain et al., 2018; Hyenne et al., 2019) and observed that stably arrested 4T1 cells efficiently interacted with platelets with an activated morphology (filopodia, Fig.2H) and endothelial cells. Altogether, this provides the first in vivo demonstration that platelet binding to TCs is efficient and can be probed at nanoscale (CLEM) and that platelet binding favors the intravascular arrest of circulating TCs.

To further document in vivo that TCs do not equally bind platelets (Fig.1), we analyzed TC-platelet binding in mouse lung sections containing early-seeded (15 mpi and 2 hpi) 4T1 or B16F10 TCs (Fig.S3A). While imaging at 15 mpi allows catching the very initial in vivo behavior of both cell lines, around 50% of the input cells are already cleared from 4T1-injected lungs after 2 hpi in the absence of platelets (please refer to Fig.2C-D), thus identifying a critical platelet-dependent step. 3D high-resolution imaging at 15 mpi revealed that 4T1 cells bind, recruit and aggregate more platelets than B16F10 also in vivo (Fig.2I), validating in vivo our initial in vitro observations. As expected, the size (volume) and numbers of platelet aggregates were also significantly lower in thrombocytopenic animals (Fig.S3B). At 2 hpi, the number of platelets found near B16F10 cells increased significantly (Fig.2J) suggesting that platelets are passively recruited in vivo to arrest sites, by either blood flow clogging or additional recruitment mechanisms. When probing cell survival using cell morphometrics, we observed increased nuclear fragmentation in both 4T1 α-GPIb-treated animals and all B16F10 mice conditions at 2 hpi (Fig.S3C-D) suggesting that these cells were non-viable. While both cell lines displayed equivalent in vitro viability up to 90 min (Fig.S3A, lower panels), the number of non-viable 4T1 cells (with fragmented nuclei) was strongly increased in absence of platelets (Fig.S3D, lower panels) suggesting that platelets favor intravascular survival of 4T1 cells, as previously reported (Labelle Hynes, 2012). Interestingly, B16F10 cells, that bind platelets poorly (in vitro and at 15 mpi in vivo), passively recruit platelets at 2 hpi (Fig.S3E) suggesting that they could favor their intravascular survival.

In conclusion, using a novel and careful in vivo analysis of early lung metastatic seeding in mice, in combination with an experimental metastasis model in zebrafish embryos, we demonstrate that platelets favor the intravascular arrest and survival of TCs. We show that platelets can either directly bind to tumor cells or passively recruit them upon arrest. As such, they do not equally promote metastatic seeding as 4T1 cells seed the lungs more efficiently than B16F10 cells (Fig.2D).

Platelets control metastatic fitness at early stages.

Having demonstrated that platelet binding efficiency correlates with intravascular arrest and survival driving efficient lung seeding, we next wondered whether such early steps would translate into efficient metastatic outgrowth. We longitudinally tracked metastatic burden over time in control and thrombocytopenic mice after a single treatment with of α-GPIb antibody prior TCs injection (14 days, Fig.3A). Because platelet counts quickly recovered and reached approximately 50% of the normal numbers at day 7, overpassing

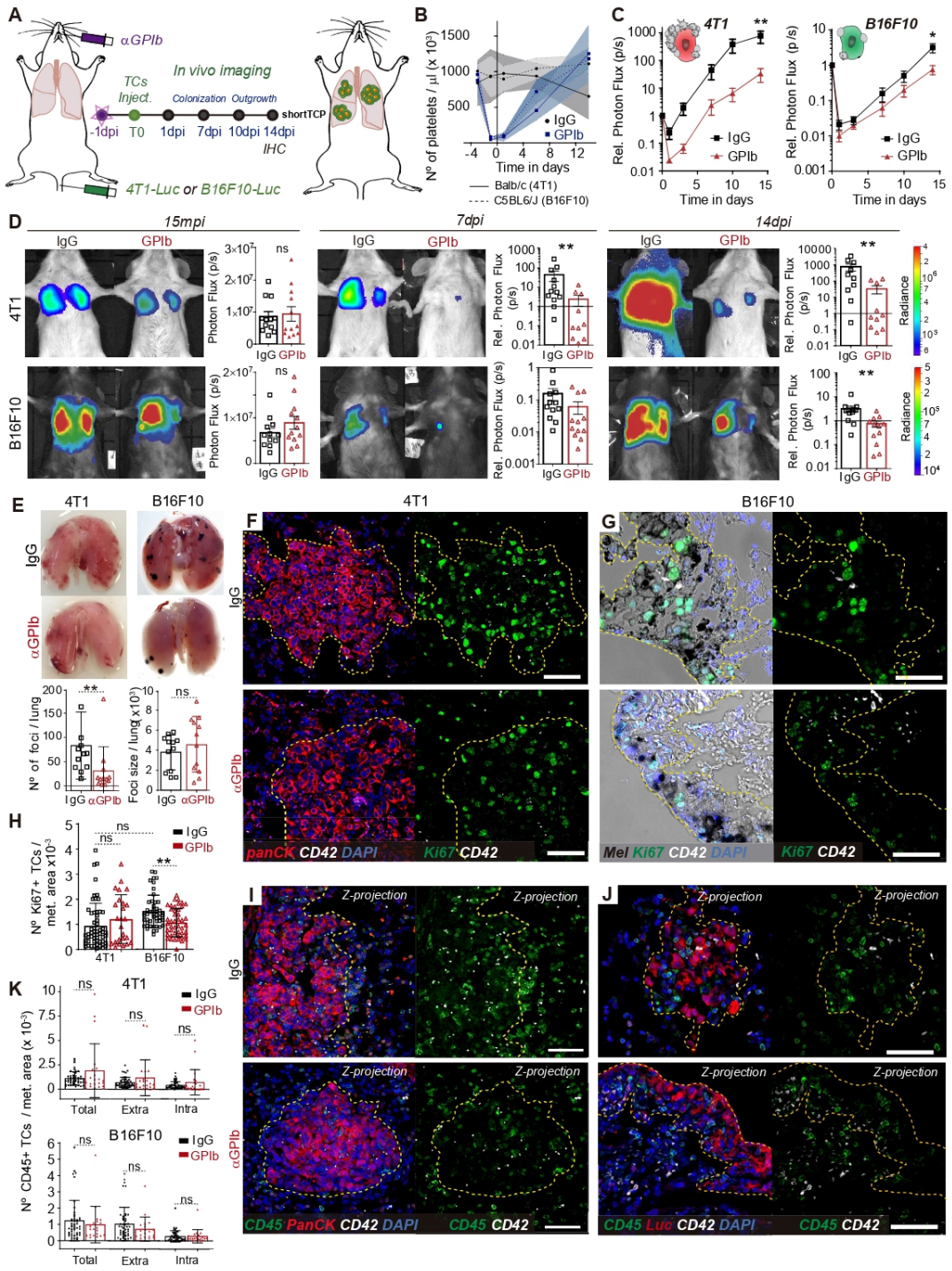

Fig. 3. Long-term TCs metastatic potential is defined by the early TC–Platelet interplay (A) Infographics showing the experimental setting to study the full metastatic cascade (14 days) in the presence or absence of platelets. 4T1-Luc or B16F10-Luc TCs are injected intravenously in normal or thrombocytopenic (TCP) mice treated with only one injection of IgG isotype control or a platelet-depleting antibody against GPIb just 24 hours prior to TCS injection. Lung seeding is followed by in vivo bioluminescence and analysis of lung metastatic foci is performed by immunohistochemistry at 14 days post-injection (14dpi). (B) Graph showing platelet counts on IgG- and GPIb-treated Balb/c and C5BL6/J animals. (C) Bioluminescence kinetics of 4T1-Luc and B16F10-Luc TCs lung seeding and outgrowth in normal and short-term TCP mice. Two-way Anova with false discovery rate post-test, mean +/-SEM, 2 independent experiments of n=5. (D) Representative images and time point (15mpi, 7dpi, and 14dpi) comparisons of total lung bioluminescence in normal versus shortTCP animals in 4T1 (up) and B16F10 (down) TCs models. Data are represented as mean +/- SEM, Mann-Whitney analysis. (E) Macroscopic analysis of mice lungs at 14dpi. Pictures of normal and α-GPIb-treated lungs with 4T1 or B16F10 metastatic foci are shown in the left panel. Graphs show the results of B16F10 foci number (left) and size (right). Data are represented as mean +/- SD of 16 mice per group from 2 independent experiments, Mann-Whitney analysis. (F) Immunohistochemical analysis of normal and shortTCP mice lungs at 14dpi seeded with 4T1. Images show paraffin sections stained with the proliferation marker Ki67 (green) and the platelet receptor CD42b (white). Scale bar: 50µm. (G) As (F), but with B16F10 TCs seeding. (H) Quantification of the proliferative capacity of both 4T1 and B16F10 metastases in control and shortTCP animals. Bar graphs show the total number of Ki67+ cells per metastatic area defined by α-pan-cytokeratin (4T1) staining or intrinsic melanin expression (B16F10). Data are represented as the mean +/- SD of 10 images or more per mice from a total of 3 to 5 mice, from 2 independent experiments, Mann-Whitney analysis. (I) Immunohistochemical analysis of normal and shortTCP mice lungs at 14dpi seeded with 4T1 or B16F10 TCs. Quantification of the immune cell recruitment within and around both 4T1 and B16F10 metastases in control and shortTCP animals was performed by co-staining tissue parafine slides with α-CD45 (green) and α-CD42b antibodies (white). (J) As (I), but with B16F10 TCs seeding. (K) Bar graphs showing the total, intrametastatic and extrametastatic number of CD45+ cells per metastatic area defined by α-pancytokeratin (4T1, top) or α-luciferase stainings (B16F10, bottom). Data are represented as the mean +/- SD of 10 or more images per mice, from a total of 2 to 3 mice from 2 independent experiments, Mann-Whitney analysis

values observed in control animals at day 14 (Fig.3B), we refer to this first experimental model as short-term thrombocytopenia (shortTCP).

Metastatic outgrowth (day 14) was significantly reduced by shortTCP in both models (Fig.3C). Interestingly, while the overall effect of shortTCP on 4T1 metastatic outgrowth was a consequence of its effect on early lung seeding (24 hpi and Fig.2), shortTCP mostly impacted the growth of B16F10 metastases only starting from 3dpi. Indeed, although lung seeding was equivalent at 24hpi of B16F10 TCs (Fig.2C-D, 3C-D), the metastatic burden was significantly reduced by shortTCP (14dpi, Fig.3C-D). While we cannot exclude that metastatic outgrowth is impacted by the quick recovery of the platelet counts (Fig.3B), these data demonstrate that platelets control early events of metastatic outgrowth of 4T1 (day 1) that later translate into a significant reduction of metastatic burden (day 14). Yet, these data also hint at an additional effect of platelets as can be observed in the low-bind B16F10 model where thrombocytopenia has no effect on lung seeding (day 1) and yet translates into significant metastasis impairment at day 14.

To gain further insight into the mechanisms that may be operating after seeding, metastatic lungs were surgically resected on day 14. Macroscopic inspection of B16F10 metastatic foci revealed, as expected, that shortTCP significantly reduced their numbers (Fig.3E, Fig.S4C), in agreement with the significantly lower bioluminescent signal observed at day 14 (Fig.3C-D). While the size of the B16F10 foci appeared similar upon shortTCP (Fig.3E), these lesions displayed a significant decrease in Ki67-positive cells indicating that their proliferation index was impacted by platelet depletion (Ki67, Fig.3G,H). Such effect was not observed in 4T1 foci (Ki67, Fig.3F,H, Fig.S4C) suggesting that platelets can tune proliferation of B16F10 during the growth of already-established metastatic foci, independently of early seeding (as short TCP had no effect). While platelets were shown to favor the recruitment of a pro-inflammatory microenvironment favoring the proliferation of TCs (Haemmerle et al., 2016), shortTCP did not affect immune cell recruitment to metastatic foci in any of the two cell models (Fig.3I,J,K). Platelets colonize and support primary tumors (Haemmerle et al., 2016; Li et al., 2014; Stone et al., 2012). Yet, whether they also populate and support metastatic foci remains to be demonstrated. We assessed the number of single (<3 platelets) or aggregated (>3 platelets) intrametastatic platelets and observed that total platelet numbers and platelet aggregates were reduced upon short TCP in both cell models (Fig.S4A), despite the recovery in platelet counts observed in shortTCP (Fig.3B). Importantly, while platelet numbers within control 4T1 and B16F10 metastases were equivalent (Fig.S4B), the number of aggregates (>3 platelets) within B16F10 metastases was significantly higher than in 4T1 metastases, suggesting that B16F10 cells are likely to better recruit, activate and aggregate platelets at later stages of the metastatic cascade (Fig.S4B). Altogether, these results demonstrate that transient thrombocytopenia perturbs early seeding and metastatic outgrowth of TC that strongly binds platelets. Such transient thrombocytopenia has however no effect on the seeding of TC that poorly bind platelets intravascularly, yet it perturbs their subsequent outgrowth. Because platelet aggregates efficiently populate metastatic foci and shape their proliferation index independently of immune cell recruitment, it is tempting to speculate that they can shape later stages of metastatic outgrowth.

Platelets control late steps of metastatic outgrowth.

Because platelets massively populate metastatic foci (Fig.S4A), release important pro-metastatic molecules (Johnson et al., 2019; Labelle, Begum, Hynes, 2011) and to circumvent the limitations of the yet classically used shortTCP model, we designed a long-term thrombocytopenia model (longTCP). This is obtained by the sequential injection of α-GPIb mAb every three to four days, starting 24h before TCs injection (Fig.4A). Doing so, we could maintain platelet counts low up to day 10 post-injection (Fig.4B) and therefore fully impair platelets interactions during the initial growth phase of micro-metastatic foci. Metastatic outgrowth of 4T1 cells was also reduced in longTCP (Fig.4C-D) when compared to shortTCP (Fig.3C-D) confirming that platelets strongly contribute to the early steps of the metastasis cascade in that model. In sharp contrast, longTCP massively impaired metastatic outgrowth of B16F10 (Fig.4C-D). While shortTCP reduced metastasis by 3-fold, longTCP reduced it by 45-fold, further emphasizing the additive effect of depleting platelets at late stages of metastasis. While lungs are equally seeded in the presence and absence of platelets (Fig.4C,D, 15 mpi), as expected from previous experiments, longTCP completely abrogates the growth of B16F10 cells resulting in metastases-free lungs at 14 dpi (Fig.4C, D, E, Fig.S5B). When combined with the observation that platelets are passively recruited by B16F10 cells at 2 hpi (Fig.2) and that they massively populate metastatic foci at 14 dpi (Fig.3), this result suggests that platelets may tune metastatic outgrowth independently of the early intravascular interaction with TCs.

To further test this hypothesis, we experimentally depleted platelets after the seeding and establishment of metastatic foci. To do so, we decreased platelet counts to only 3dpi of B16F10 with three successive injections of α-GPIb until day 10 (Fig.4A, bottom). We named this experimental approach lateTCP. It allows, for the first time, to control platelet counts after the initial growth of metastatic foci and to interrogate a novel contribution of platelets to metastatic outgrowth (Fig.4F). Interestingly, lateTCP on B16F10-seeded lungs significantly reduced metastatic outgrowth from day 7 (Fig. 4G-H), thus confirming that platelets are capable of controlling the growth of already-established and growing metastatic foci. Indeed, while the number of foci in control and α-GPIb-treated mice was similar, their size was significantly reduced in lateTCP (Fig.4I, Fig.S5C) as expected from the effect of lateTCP on B16F10 cell proliferation index (Fig.4J,M). While recruitment of CD45-positive cells remains unchanged upon this lateTCP (Fig.4K), we again observed that the number of intrametastatic platelets was significantly reduced when depleting platelets only 3 dpi (Fig.4L)

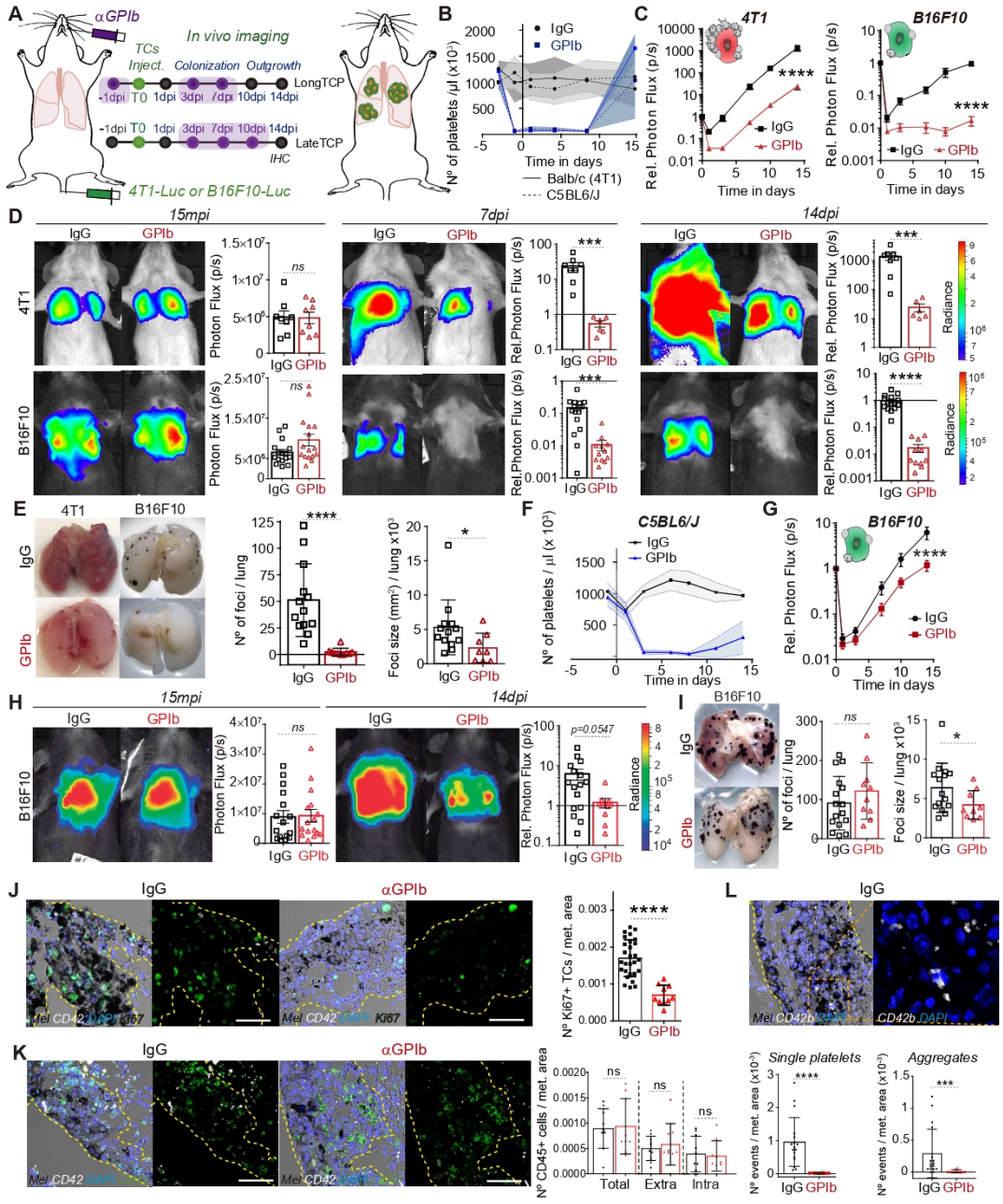

Fig. 4. Platelets significantly influence the late outgrowth of B16F10 metastatic foci but not 4T1 ones (A) Infographics showing the experimental setting to study the late events of the metastatic cascade (14 days) in the presence or absence of platelets. 4T1-Luc or B16F10-Luc TCs are injected intravenously in normal or thrombocytopenic (TCP) mice treated with 3 injections of IgG isotype control or a platelet-depleting antibody against GPIb at different time points. (B) A first set of mice were injected before and after 4T1 or B16F10 TCs injection to maintain platelet counts low during the whole experiment (longTCP). (C) Bioluminescence kinetics of 4T1-Luc (left) and B16F10-Luc (right) TCs lung seeding and outgrowth in control and long-term TCP mice. Two-way Anova with false discovery rate post-test, mean +/- SEM, 2 independent experiments of n=4. (D) Representative images and time point quantifications (15mpi, 7dpi and 14dpi) of total lung bioluminescence in control versus longTCP animals in 4T1 (up) and B16F10 (down) TCs models. Mean +- SEM, Mann-Whitney analysis. (E) Macroscopic analysis of mice lungs at 14dpi. Pictures of normal and α-GPIb-treated lungs with 4T1 or B16F10 metastatic foci are shown in the left panel. Graphs show B16F10 foci number (middle) and mean foci size (right). Mean +/- SD of 16 mice per group from 1 (4T1) or 2 (B16F10) independent experiments, Mann-Whitney analysis. (F) Following (A), a second set of mice were injected only after B16F10 TCs injection, to deplete platelets after TCs seeing in the lungs (lateTCP). (G) Kinetics of B16F10-Luc TCs lungs outgrowth in control and lateTCP mice. Two-way Anova with false discovery rate post-test, mean +/- SEM, 2 independent experiments of n=4. (H) Representative images and time point comparisons (15mpi and 14dpi) of total lung bioluminescence in control versus lateTCP animals in B16F10 TCs models. Mean+- SEM, Mann-Whitney analysis. (I) Macroscopic analysis of mice lungs at 14dpi. Pictures of normal and α-GPIb-treated lungs with B16F10 metastatic foci are shown in the left panel. Graphs show the results of B16F10 foci number (middle) and mean foci size (right) . Mean +/- SD, 8 mice per group from 1 experiments. Immunohistochemical analysis of control and lateTCP mice lungs at 14dpi seeded with B16F10 TCs. (J) Representative images of proliferative (α-Ki67, green, left) and graph quantification (right) from 10 images per mice from 2 to 3 mice, 2 independent experiments, mean +-SD, Mann-Whitney analysis. (K) Representative images of CD45 immune positives cells (α-CD45, green, left) and graph quantification (right) of cell numbers presented as total, extrametastatic (surrounding) or intrametastatic CD45+ cells, from 8 images per mice from 2 to 3 mice, 2 independent experiments, mean +-SD, Mann-Whitney analysis. (L) Representative images of platelets inside lungs metastases (α-CD42b, white, top) and graph quantification (bottom) as single platelet (3) or aggregates platelets (>3) from 8 images per mice from 2 to 3 mice, 2 independent experiments, mean +-SD, Mann-Whitney analysis.

suggesting that recruitment and density of platelets within metastatic foci is crucial for their outgrowth. To further support the pro-metastatic contribution of platelets to established metastatic foci, we next interrogated whether platelets would also populate human metastatic foci. With that aim, we analyzed human lung metastasis biopsies from metastatic melanoma patients and found that platelets could easily be detected within metastatic foci (Fig.S5A). Altogether, these results provide the first evidence that platelets can populate human metastatic foci, further suggesting that they may control metastasis at the late stages of their progression. They further open the possibility that targeting platelets in already established metastasis colonies could impair metastasis growth.

Platelets control late steps of metastasis via GPVI.

The late contribution of platelets to metastatic outgrowth opens a promising therapeutic window that could circumvent the current limitations in impairing metastatic extravasation or in detecting early metastatic foci that often occurs even before cancer detection (Hu et al., 2019; Husemann et al., 2008). Yet, one needs to identify the molecular targets involved and design a strategy that would avoid deleterious thrombocytopenic effects while impairing the outgrowth of established metastases. To do so, we first exploited in-house genetic models that allow us to test the contribution of a specific platelet receptor, namely the collagen and fibrinogen receptor GPVI. GPVI is an immunoglobulin (Ig)–like glycoprotein which binds to many different adhesive proteins and that (Jandrot-Perrus et al., 2000) stimulates platelet aggregation by activating of GPIIb/IIIa integrins. Recent studies placed it as an attractive candidate in the promotion of platelet-dependent metastasis (Mammadova-Bach et al., 2020; Tesfamariam Wood, 2022), notably because of the minimal impact of its depletion on bleeding. Whether it also tunes late steps of metastasis remains to be demonstrated.

To allow for syngeneicity in the GPVI-/- mouse model with two breast and melanoma cell lines (Fig.5A), we engineered the mouse breast cancer AT3 (give details and refs) cell line for stable luciferase expression to mirror the previously used 4T1 model, as these cells also displayed a high platelet-binding capacity (Fig.1A). Interestingly, the metastatic outgrowth of high-bind AT3 cells remained unaltered in the absence of GPVI (Fig.5B-C). Similarly, when targeting GPVI pharmacologically with a GPVI-depleting antibody (JAQ.1, Emfret, Fig.S6A,D) that allows maintaining normal platelet counts (Fig.S6A,B), lung seeding (1 dpi) and metastatic outgrowth (14 dpi) of high-bind 4T1 cells remained unaffected (Fig.S6C,E-F) suggesting that targeting GPVI might be inefficient for TC that strongly bind platelets and whose metastatic behavior is shaped by early intravascular platelet-TC interactions.

In contrast, the metastatic progression of B16F10 was significantly reduced in the absence of the GPVI receptor (Fig.5B-C). While seeding of B16F10 appeared again unaffected (1 dpi), metastatic outgrowth was progressively impaired over time, starting from day 7 (Fig.5B-C), as we had observed in the longTCP model (Fig.4G-H). Macroscopic analysis of metastatic lungs revealed again that the number of foci was similar in both conditions, while their size (and proliferation index) was significantly reduced in absence of GPVI (Fig.5D,E). In addition, the number of intrametastatic platelets found was significantly reduced in GPVI-/- mice (Fig.5F). Interestingly their activation ability, measured by the number of aggregates found was not affected. Altogether, these results suggest that the platelet receptor GPVI shapes metastatic outgrowth of TCs that do not rely on early intravascular platelet-TC interactions, without impacting the lung seeding abilities of TCs. It further emphasizes the need to consider platelet binding efficiencies and molecular targets before designing platelet-targeted anti-metastatic strategies. Nevertheless, they allow us to validate GPVI as an ideal target. Its minimal effect on bleeding and its contribution to late steps of tumor metastasis make it an appealing candidate for testing its anti-metastatic potential in a human-relevant context.

Targeting the human GPVI receptor with a humanized antibody impairs metastasis.

While this study and others (reviewed in Tesfamariam Wood, 2022) confirm that GPVI is a promising target for impairing metastasis, its relevance to human pathology is missing. Thus, better preclinical models and humanized therapeutic tools, with ideally no thrombocytopenic effects, are needed. To do so, we exploited our previously established genetically modified mouse strain expressing human GPVI (hGPVI, Mangin et al., 2012). While these mice are viable with no hematological defects, they express a knock-in copy version of hGPVI that makes it the best candidate to test anti-GPVI compounds. To counteract GPVI function, we decided to exploit Glenzocimab (previously ACT017, Acticor Biotech, Lebozec et al. 2017), a humanized antibody fragment (Fab) that has recently completed a phase II trial in stroke patients (Acute Ischemic Stroke Interventional Study "ACTIMIS", clinicaltrials gov. Identifier: NCT03803007). This compound binds to hGPVI to block ligand binding, which, most importantly, occur without causing thrombocytopenia or depletion of GPVI, and are not associated with bleeding events (Jadoui et al., 2021).

Building on the exciting observation that lateTCP could reduce the growth of established metastases (Fig.4), we subjected hGPVI mice to an experimental metastasis protocol targeting the growth of established metastases (mimicking lateTCP, Fig.5G). The half-life of Glenzocimab in mice is rather short (data not shown) when compared to humans (Jadoui et al., 2021; Voors-Pette et al. 2019). We thus administrated Glenzocimab progressively using osmotic pumps that were implanted subcutaneously (Fig.5G). We confirmed that Glenzocimab did not affect platelet counts (Fig.5H) and was found to be successfully bound to mouse platelets (Fig.5L) four days after pump implantation. Longitudinal imaging of B16F10 lung metastasis revealed that the metastatic burden of hGPVI mice treated with Glenzocimab was significantly reduced starting from 4 days after the implantation of the pump (Fig.5I,J). Metastasis growth was constantly reduced, reaching a 4-fold decrease at 14 dpi (Fig.5I). Macroscopic

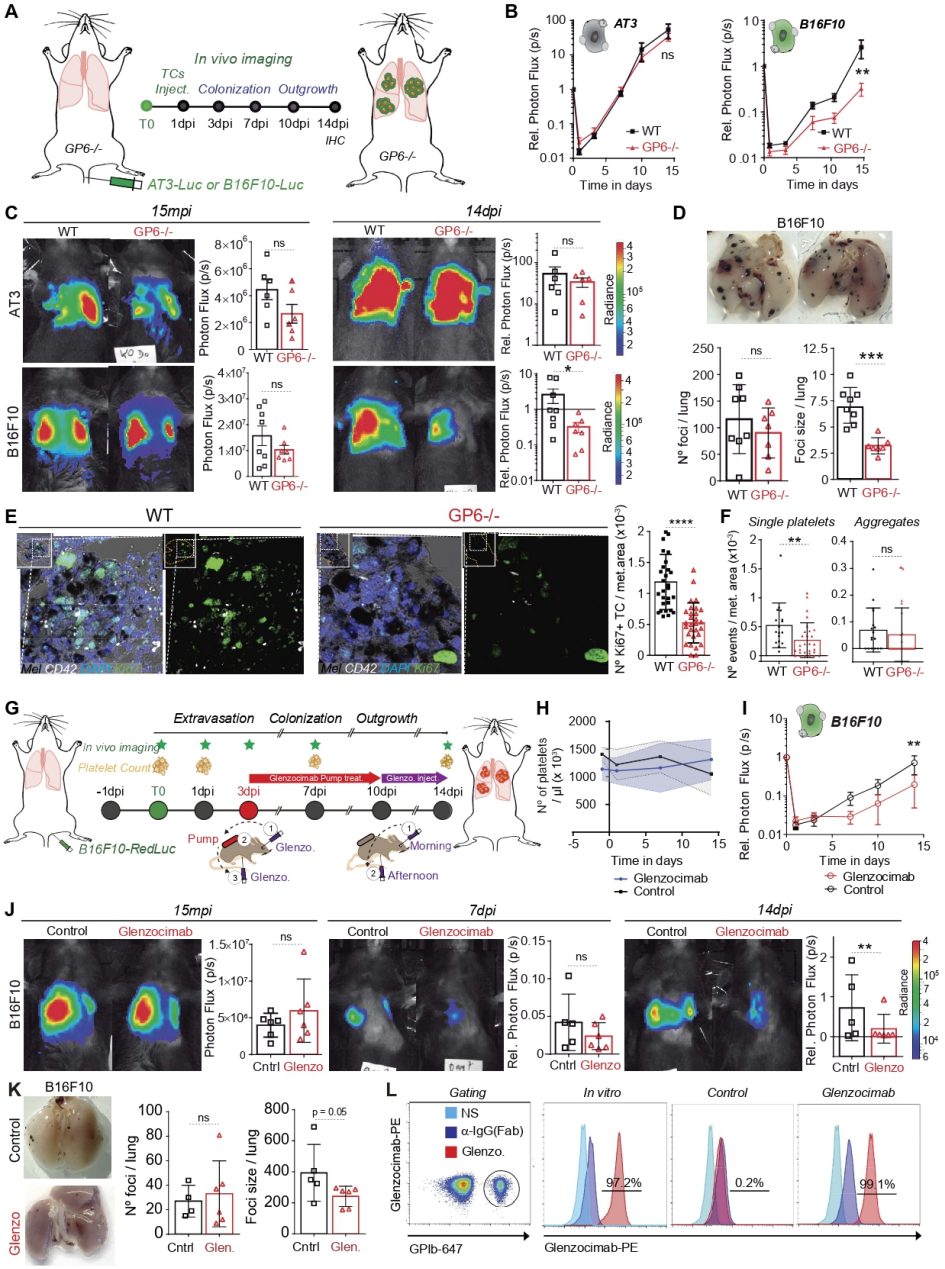

Fig. 5. Therapeutic targeting of the human GPVI receptors impairs metastatic outgrowth of established foci (A) Infographics showing the experimental setting to study the role of GPVI platelet receptor in GPVI KO mice along 14 days. AT3-Luc or B16F10-Luc TCs are injected intravenously in WT or GPVI KO mice. Lung seeding and metastatic outgrowth is followed by in vivo bioluminescence. (B) Bioluminescence kinetics of AT3-RedFluc-L2 and B16F10-Luc TCs lung outgrowth in wild type and GPVI KO mice. Two-way Anova with false discovery rate post-test, mean +/- SEM. (C) Representative images and time point (15mpi on the left; 14dpi on the right) comparisons of total lung bioluminescence in normal versus GPVI-depleted animals in AT3 (up) and B16F10 (down) TCs models. Data are presented as the mean +/- SEM, Mann-Whitney analysis. (D) Macroscopic analysis of mice lungs injected with B16F10 cells at 14dpi. Pictures of normal (left) and GPVI-deficient (right) lungs are show. Graphs show the results of B16F10 foci number (bottom left) and size (bottom right) analysis performed on ImageJ. Data are represented as mean +/- SD of 8 mice per group from 1 independent experiment. (E) Representative zoomed images of the immunohistochemical analysis of lung tissue sections containing B16F10 metastatic foci. Scale =50µm. Proliferative cells within metastatic foci are labelled using the Ki67 marker (green) and platelets with an anti-CD42b antibody (white). Graph data (right) are presented as the mean +/- SEM, Mann-Whitney analysis. (F) Graph shows the number of intrametastatic platelets per metastatic area in control and GPVI-deficient animals. Data are represented as mean +/- SD of 10 or more images per mice per group, from 2 to 3 mice and from 1 experiment, Mann-Whitney analysis. (G) Infographics showing the experimental setting to study the impact of GPVI blockade in the outgrowth of B16F10 lung metastasis. B16F10-Luc TCs are injected intravenously in control or α-hGPVI Fab-treated mice (Glenzocimab). Due to the short half-life of the Glenzocimab in mice, the administration is performed by a constant delivery via subcutaneous osmotic pumps. The pumps are implanted 3 days post TCs injection to ensure the establishment of micro-metastatic foci. In this setting TCs outgrowth is followed by in vivo bioluminescence and analysis of lung metastatic foci is performed by macroscopic inspection at 14 days post-injection (14dpi). (H) Graph showing platelet counts on control and Glenzocimab-treated animals. (I) Bioluminescence kinetics of B16F10-Luc TCs lung outgrowth in normal and short-term TCP mice. Two-way Anova with false discovery rate post-test, mean +/- SEM, 2 independent experiments of n=3. (J) Representative images and time point (15mpi, 7dpi and 14dpi) comparisons of total lung bioluminescence in control versus Glenzocimab-treated animals. Data are represented as mean +/- SEM, Mann-Whitney analysis. (K) Macroscopic analysis of mice lungs at 14dpi. Pictures of control (top) and α-hGPVI-treated (bottom) lungs with B16F10 metastatic foci are shown. Graphs show the results of B16F10 foci number (middle) and size (right). Data are represented as mean +/- SD of 6 mice per group from 2 independent experiments. (L) Flow cytometry analysis of mouse platelets labelled in vitro and in vivo. First histogram refers to the electronic gating strategy on platelets labelled with α-GPIb-647. Second histogram refers to platelets stained with Glenzocimab plus an anti-human (Fab) –PE-labelled antibody in vitro. Two last histograms refer to mouse platelets from control or Glenzocimab-treated animals stained with the anti-human (Fab) – PE-labelled antibody.

inspection of the lungs revealed that Glenzocimab had, as expected, no effect on the number of metastatic foci that are initiated before the start of the treatment, but significantly reduced their size (Fig.5K). Altogether, these results identify, for the first time, an anti-GPVI compound that can target the human version of GPVI and impair metastatic progression with no side effects (thrombocytopenia, bleeding). Considering the very positive safety profile of Glenzocimab and its efficiency in repressing growing metastasis, we provide here a new therapeutic agent with previously unmet clinical potential.

DISCUSSION

This manuscript reports the first longitudinal analysis on the pro-metastatic role of platelets in lung metastasis by subjecting two tumor cell models (breast carcinoma and melanoma) to experimental metastasis assays in the zebrafish embryo and in mice. These were tested in six mouse models of time-controlled thrombocytopenia and by the genetic and pharmacological ablation of the platelet receptor GPVI. By these means, we have discovered that different cancer cells interact with platelets differently, tuning their intravascular arrest and metastatic fitness. Importantly, we provide the first study demonstrating the therapeutic efficacy of targeting the platelet receptor GPVI in animals carrying growing metastases and further identifies GPVI as the first molecular target whose inhibition can impair metastasis without inducing collateral hemostatic perturbations.

The established mechanisms proposed for the pro-metastatic role of platelets including platelet binding, activation, and aggregation by TCs, have been traditionally insufficient in providing momentum for the development and establishment of anti-platelet drugs in routine oncologic care. This may lie in the exclusive focus in a too narrow and early window within the metastatic process, thus leaving few options for therapeutic intervention. Additionally, current data assume that all cancers interact equivalently with platelets, which might lead to controversial results in different cancer models (Erpenbeck et al., 2010) (Echtler et al., 2017) and unclear outcomes when using anti-platelet drugs in oncologic patients (reviewed in (Lucotti Muschel, 2020)). For example, thrombocytosis is a poor prognosis factor, reflecting an aggressive tumor phenotype in cervical, colon, and non-small cell lung cancer patients. (Gao, Zhang, Zhang, Zhang, Wang, 2017; Wang et al., 2017). On the contrary, in pancreatic cancer, thrombocytopenia was associated with a worse prognosis, thus indicating the varied influence of platelets depending on the type of cancer (Schwarz, 1999) (Wojtukiewicz, Sierko, Hempel, Tucker, Honn, 2017)). While CTCs are widely considered to be covered by platelets when entering the blood (Labelle Hynes, 2012), whether this applies to all cancer types or cells remains to be demonstrated. Here, we show that TCs types do not all bind platelets equally (Fig.1) and importantly, TCIPA seems to occur only at high concentrations of TCs in vitro (Alonso-Escolano, Strongin, Chung, Deryugina, Radomski, 2004; Jurasz, Alonso-Escolano, Radomski, 2004; Katagiri et al., 1991), which is an unlikely scenario in vivo. All these issues have left anti-platelet drugs out of the standard cancer treatments and/or prophylaxis. Aware of this, and the lack of longitudinal studies of the whole lung metastatic cascade in vivo, we developed a novel experimental approach merging the single cell analysis of in vivo arrested TCs combined with in vivo bioluminescence longitudinal analysis of micro- and macro-metastases. This approach allowed us to identify a novel pro-metastatic role of platelets in the late stages of the disease mediated by the GPVI platelet receptor, and allowed us to probe the feasibility of targeting it with a therapeutic antibody.

By the above-mentioned means, first, we identified differential platelet binding profiles in different TC types. We are aware that our binding results may not mimic physiological conditions, but this simple approach proved to be a good starting point to enquire about the specific interaction of platelets and different tumor cells in more complex models integrating blood flow forces. Indeed, static binding profiles correlated with the in vivo pro-metastatic effects observed in both ZF and mouse, although their absolute binding efficiencies differed. It has been shown that hydrodynamic shear affects the receptor specificity of activation-dependent platelet binding to TCs, as evidenced by the transition from a P-selectin-independent/Arg-Gly-Asp (RGD)-dependent process at 100 s-1 to a P-selectin/αIIbB3-dependent interaction at 800 s-1 (McCarty, Jadhav, Burdick, Bell, Konstantopoulos, 2002). This may imply that static assays such as SEM or aggregations are overestimating platelet binding, as in such a scenario resting platelets could bind independently of P-selectin and αIIbB3 integrin. On the contrary, in an in vivo situation under flow, platelets must be activated to bind TCs, so regions of low flow in vivo may increase platelet binding through this P-selectin/αIIbB3 independent mechanism. In this sense, it is interesting to notice that platelets are most pro-metastatic in the model able to bind more platelets in static conditions (4T1 cells), meaning that low flow binding abilities are capital for tuning TC's metastatic fitness. In this line, we can observe in our ZF data that platelets favor the stable adhesion of 4T1 cells exclusively, indicating that an early and active platelet binding is capital for the arrest of TCs in blood vessels that aren't physically constraining to TCs. The putative molecular players involved in this differential binding remain to be investigated.

To further understand the mechanisms driving the pro-metastatic effect of platelets at early stages, we performed an exhaustive analysis by quantitative confocal imaging of single cells arrested in mouse lungs. This allowed us to characterize the dynamics of the arresting site and probe TCs viability and platelets recruitment. We first confirmed that binding profiles found in vitro in static conditions are conserved in vivo (when comparing binding efficiencies of 4T1 and B16). The platelet binding profile changed only 2 hours post-injection, with B16F10 cells now attracting increasing numbers of platelets. Platelets favour the survival of intravascularly arrested TCs by direct binding to the surface of viable cells or by passive recruitment around non-viable cells. This passive recruitment may occur by vessel occlusion or

release of platelet-activating cytoplasmic content such as tissue factor (TF) (Feinauer et al., 2020; Monroe Key, 2007). In the first case, active recruitment leads to a highly significant long-term metastatic fitness enhancement (Fig.3), while in the latter case, passive recruitment leads to a discrete but significant metastatic fitness enhancement, only appreciated at late time points (14dpi). Previous work has suggested a key role for thrombin and clot formation as the starting point of brain metastasis (Feinauer et al., 2020), however, not all metastatic cell lines express TF, the trigger of thrombin generation. Considering that metastasis is a very inefficient process and that intravascular cell death is a well-known cause for TF release and thrombin production, the co-option of viable with non-viable cells may help the viable cell to successfully metastasize, as previously observed (Allen et al., 2014). Anyhow, this difference between active and passive platelet recruitment mechanisms may be capital for the design of drugs to avoid platelet recruitment and activation at the arrest and thus outgrowth sites in different cancer types.

Previous reports have found evidence of platelets inside primary tumors (Haemmerle et al., 2016; Li et al., 2014; Stone et al., 2012) with no evidence that this could apply to metastasis. We now document that metastatic platelets are heavily populated by platelets stably bound to growing metastatic cells suggesting that they might be able to extravasate with or independently of TCs as reported previously (Sood et al., 2006). Platelets have been shown to migrate easily within tissues (Gaertner et al., 2017) suggesting that they could actively populate growing metastases. Whether platelets require extravasation to seed metastases remains to be demonstrated. Platelets might interact at early stages may imprint TCs, thus tuning their metastatic potential. For example, while TCs are accompanied by platelets, fibrin, or fibrinogen from 0 to 6h post-injection, platelets cannot be found at intravascular arresting site from 6 to 24 hpi (Wojtukiewicz et al., 2017). It is thus likely that the GPVI receptor may tune the proliferative advantage showed in our genetic and pharmacological GPVI loss-of-function models at very early steps of the cascade.

Whether platelets actively migrate and exchange material within metastatic foci remains to be demonstrated and opens exciting avenues of research, the observation that only the number of platelets but not their aggregation capacity within the tumors is affected in GPVI KO animals (Fig.5F) may indicate a defect in migration. It further confirms the safe thrombostatic profile of GPVI-targeted platelets in vivo at cellular level. Platelets are known to release significant amounts of bioactive material within releasates (Lazar Goldfinger, 2021) that shape, for example, their invasion abilities. Platelets also secrete microparticles and extracellular vesicles, which are immunosuppressive (Haemmerle, Stone, Menter, Afshar-Kharghan, Sood, 2018) and enhance TCs survival and outgrowth capacity (Vismara et al., 2021). However, although we have confirmed an increased proliferative index in the presence of platelets in all our TCP models, we have not been able to see differences regarding immune cells' recruitment into metastases. A deeper analysis characterizing the nature and functional phenotype of immune cell infiltrates in TCP models would help to clarify this issue and provide clues as to what triggers metastatic impairment when targeting GPVI.

While reducing platelet count is not a viable therapeutic approach, due to the risk of bleeding, targeting some platelet receptors could circumvent this issue. When depleting or targeting GPVI, we could indeed successfully impair the proliferation rate within B16F10 metastatic foci. This points to GPVI as a promising target to develop new anti-metastatic drugs able to target the disease once the metastatic spread is already initiated, which account most of the cases in clinical practice. Such achievement is of utmost importance. Amongst the platelet specific receptors, two of them, the GPIb-V-IX complex, and GPVI appear to play a very important role in tumor metastasis. We provide here evidence that a pharmacologic blockade of GPVI with glenzocimab (Acticor Biotech), an anti-GPVI agent evaluated in clinical trials to prevent ischaemic stroke, efficiently reduces experimental metastasis. This drug is particularly promising as it has an anti-thrombotic effect without inducing any bleedings in healthy volunteers and in patients (Glenzocimab is a humanized antibody fragment (Fab) that has been proved safe in phase I clinical trial in healthy volunteers (Voors-Pette et al., 2019)). While there are several anti-platelet drugs available in the market, most of them increase the risk of hemorrhage in clinical settings, or have limited efficacy against metastasis, with the exception of aspirin (Tao, Tassi Yunga, Williams, McCarty, 2021). Altogether, our recent work demonstrates that targeting platelets in animals carrying growing metastases can impair them. It further identifies GPVI as the first molecular target whose inhibition can impair metastasis without inducing collateral hemostatic perturbations.

ACKNOWLEDGMENTS and FUNDING

We thank all members of J.G.G's team for their constant discussions on this particular topic. J.G.G is the coordinator of the NANOTUMOR Consortium, a program from ITMO Cancer of AVIESAN (Alliance Nationale pour les Sciences de la Vie et de la Santé, National Alliance for Life Sciences Health) within the framework of the Cancer Plan (France). Work and people in the lab of J.G.G. are mostly supported by the INCa (Institut National Du Cancer, French National Cancer Institute), charities (La Ligue contre le Cancer, ARC (Association pour la Recherche contre le Cancer), FRM (Fondation pour la Recherche Médicale)), the National Plan Cancer initiative, the Region Grand Est, INSERM and the University of Strasbourg. This work has been directly funded by the INCa grant (PLBIO 2014-01) and by the support of the Ligue contre le Cancer (labelisation) and the SATT Conectus (Strasbourg). MGL has been funded by the University of Strasbourg (IdeX, investissements d'Avenir), the INCa and the SATT Conectus (Strasbourg). MP is supported by INCa, FC by NANOTUMOR and VM by a Ph.D. fellowship from the French Ministry of Science (MESRI). GF was supported by La Ligue contre le Cancer. We are grateful to Martine Jandrot-Perrus for the initial work regarding Glen-

zocimab and the hGPVI mice, to Acticor for providing the Glenzocimab and to François Bertucci for providing human samples. We are also thankful for recent donators (Rohan Athlétisme Saverne) to support our work.

ETHICS STATEMENT

Human studies were performed according to Helsinki declaration. Control human samples were obtained from volunteer blood donors who gave written informed consent recruited by the blood transfusion center where the research was performed (Etablissement Français du Sang, Grand-Est). All procedures were registered and approved by the French Ministry of Higher Education and Research. The donors gave their approval in the CODHECO number AC-2008 - 562 consent form, for the samples to be used for research purposes. Immunocompetent and genetically modified mice used in this study were housed under pathogen-free conditions and all procedures were performed in accordance with the European Union Guideline 2010/63/EU. The study was approved by the Regional Ethical Committee for Animal Experimentation of Strasbourg, CREMEAS (CEEA 35) and registered under the APAFIS authorization 14741-2018041816337540.

REFERENCES

Aceto, N., Bardia, A., Miyamoto, D. T., Donaldson, M. C., Wittner, B. S., Spencer, J. A., . . . Maheswaran, S. (2014). Circulating tumor cell clusters are oligoclonal precursors of breast cancer metastasis. Cell, 158(5), 1110-1122. doi: 10.1016/j.cell.2014.07.013

Aigner, S., Sthoeger, Z. M., Fogel, M., Weber, E., Zarn, J., Ruppert, M., . . . Altevogt, P. (1997). CD24, a mucin-type glycoprotein, is a ligand for P-selectin on human tumor cells. Blood, 89(9), 3385-3395.

Aceto, N., Bardia, A., Miyamoto, D. T., Donaldson, M. C., Wittner, B. S., Spencer, J. A., . . . Maheswaran, S. (2014). Circulating tumor cell clusters are oligoclonal precursors of breast cancer metastasis. Cell, 158(5), 1110-1122. doi: 10.1016/j.cell.2014.07.013

Aigner, S., Sthoeger, Z. M., Fogel, M., Weber, E., Zarn, J., Ruppert, M., . . . Altevogt, P. (1997). CD24, a mucin-type glycoprotein, is a ligand for P-selectin on human tumor cells. Blood, 89(9), 3385-3395.

Allen, J. E., Saroya, B. S., Kunkel, M., Dicker, D. T., Das, A., Peters, K. L., . . . El-Deiry, W. S. (2014). Apoptotic circulating tumor cells (CTCs) in the peripheral blood of metastatic colorectal cancer patients are associated with liver metastasis but not CTCs. Oncotarget, 5(7), 1753-1760. doi: 10.18632/oncotarget.1524

Alonso-Escolano, D., Strongin, A. Y., Chung, A. W., Deryugina, E. I., Radomski, M. W. (2004). Membrane type-1 matrix metalloproteinase stimulates tumour cell-induced platelet aggregation: role of receptor glycoproteins. Br J Pharmacol, 141(2), 241-252. doi: 10.1038/sj.bjp.0705606

Chew, H. K., Wun, T., Harvey, D. J., Zhou, H., White, R. H. (2007). Incidence of venous thromboembolism and the impact on survival in breast cancer patients. J Clin Oncol, 25(1), 70-76. doi: 10.1200/JCO.2006.07.4393

Echtler, K., Konrad, I., Lorenz, M., Schneider, S., Hofmaier, S., Plenagl, F., . . . Schulz, C. (2017). Platelet GPIIb supports initial pulmonary retention but inhibits subsequent proliferation of melanoma cells during hematogenic metastasis. PLoS One, 12(3), e0172788. doi: 10.1371/journal.pone.0172788

Edwards, R. L., Rickles, F. R., Moritz, T. E., Henderson, W. G., Zacharski, L. R., Forman, W. B., . . . et al. (1987). Abnormalities of blood coagulation tests in patients with cancer. Am J Clin Pathol, 88(5), 596-602. doi: 10.1093/ajcp/88.5.596

Erpenbeck, L., Nieswandt, B., Schon, M., Pozgajova, M., Schon, M. P. (2010). Inhibition of platelet GPIb alpha and promotion of melanoma metastasis. J Invest Dermatol, 130(2), 576-586. doi: 10.1038/jid.2009.278

Feinauer, M. J., Schneider, S. W., Berghoff, A. S., Robador, J. R., Tehranian, C., Karreman, M. A., . . . Winkler, F. (2020). Local blood coagulation drives cancer cell arrest and brain metastasis in a mouse model. Blood. doi: 10.1182/blood.2020005710

Follain, G., Herrmann, D., Harlepp, S., Hyenne, V., Osmani, N., Warren, S. C., . . . Goetz, J. G. (2020). Fluids and their mechanics in tumour transit: shaping metastasis. Nat Rev Cancer, 20(2), 107-124. doi: 10.1038/s41568-019-0221-x

Follain, G., Osmani, N., Azevedo, A. S., Allio, G., Mercier, L., Karreman, M. A., . . . Goetz, J. G. (2018). Hemodynamic Forces Tune the Arrest, Adhesion, and Extravasation of Circulating Tumor Cells. Dev Cell, 45(1), 33-52 e12. doi: 10.1016/j.devcel.2018.02.015

Gaertner, F., Ahmad, Z., Rosenberger, G., Fan, S., Nicolai, L., Busch, B., . . . Massberg, S. (2017). Migrating Platelets Are Mechano-scavengers that Collect and Bundle Bacteria. Cell, 171(6), 1368-1382 e1323. doi: 10.1016/j.cell.2017.11.001

Gao, L., Zhang, H., Zhang, B., Zhang, L., Wang, C. (2017). Prognostic value of combination of preoperative platelet count and mean platelet volume in patients with resectable non-small cell lung cancer. Oncotarget, 8(9), 15632-15641. doi: 10.18632/oncotarget.14921

Gasic, G. J., Gasic, T. B., Stewart, C. C. (1968). Antimetastatic effects associated with platelet reduction. Proc Natl Acad Sci U S A, 61(1), 46-52.

Gkountela, S., Castro-Giner, F., Szczerba, B. M., Vetter, M., Landin, J., Scherrer, R., . . . Aceto, N. (2019). Circulating Tumor Cell Clustering Shapes DNA Methylation to Enable Metastasis Seeding. Cell, 176(1-2), 98-112 e114. doi: 10.1016/j.cell.2018.11.046

Goetz, J. G., Steed, E., Ferreira, R. R., Roth, S., Ramspacher, C., Boselli, F., . . . Vermot, J. (2014). Endothelial cilia mediate low flow sensing during zebrafish vascular development. Cell Rep, 6(5), 799-808. doi: 10.1016/j.celrep.2014.01.032

Haemmerle, M., Bottsford-Miller, J., Pradeep, S., Taylor, M. L., Choi, H. J., Hansen, J. M., . . . Sood, A. K. (2016). FAK regulates platelet extravasation and tumor growth after antiangiogenic therapy withdrawal. J Clin Invest, 126(5), 1885-1896. doi: 10.1172/JCI85086

Haemmerle, M., Stone, R. L., Menter, D. G., Afshar-Kharghan, V., Sood, A. K. (2018). The Platelet Lifeline to Cancer: Challenges and Opportunities. Cancer Cell, 33(6), 965-983. doi: 10.1016/j.ccell.2018.03.002

Headley, M. B., Bins, A., Nip, A., Roberts, E. W., Looney, M. R., Gerard, A., Krummel, M. F. (2016). Visualization of immediate immune responses to pioneer metastatic cells in the lung. Nature, 531(7595), 513-517. doi: 10.1038/nature16985

Hu, Z., Ding, J., Ma, Z., Sun, R., Seoane, J. A., Scott Shaffer, J., . . . Curtis, C. (2019). Quantitative evidence for early metastatic seeding in colorectal cancer. Nat Genet, 51(7), 1113-1122. doi: 10.1038/s41588-019-0423-x

Husemann, Y., Geigl, J. B., Schubert, F., Musiani, P., Meyer, M., Burghart, E., . . . Klein, C. A. (2008). Systemic spread is an early step in breast cancer. Cancer Cell, 13(1), 58-68. doi: 10.1016/j.ccr.2007.12.003

Hyenne, V., Ghoroghi, S., Collot, M., Bons, J., Follain, G., Harlepp, S., . . . Goetz, J. G. (2019). Studying the Fate of Tumor Extracellular Vesicles at High Spatiotemporal Resolution Using the Zebrafish Embryo. Dev Cell, 48(4), 554-572 e557. doi: 10.1016/j.devcel.2019.01.014

Jadoui, S., Le Chapelain, O., Ollivier, V., Mostefa-Kara, A., Di Meglio, L., Dupont, S., . . . Ho-Tin-Noe, B. (2021). Glenzocimab does not impact glycoprotein VI-dependent inflammatory haemostasis. Haematologica, 106(7), 2000-2003. doi: 10.3324/haematol.2020.270439

Jain, S., Russell, S., Ware, J. (2009). Platelet glycoprotein VI facilitates experimental lung metastasis in syngenic mouse models. J Thromb Haemost, 7(10), 1713-1717. doi: 10.1111/j.1538-7836.2009.03559.x

Jain, S., Zuka, M., Liu, J., Russell, S., Dent, J., Guerrero, J. A., . . . Ware, J. (2007). Platelet glycoprotein Ib alpha supports experimental lung metastasis. Proc Natl Acad Sci U S A, 104(21), 9024-9028. doi: 10.1073/pnas.0700625104

Jandrot-Perrus, M., Busfield, S., Lagrue, A. H., Xiong, X., Debili, N., Chickering, T., . . . Villeval, J. L. (2000). Cloning, characterization, and functional studies of human and mouse glycoprotein VI: a platelet-specific collagen receptor from the immunoglobulin superfamily. Blood, 96(5), 1798-1807.

Johnson, K. E., Ceglowski, J. R., Roweth, H. G., Forward, J. A., Tippy, M. D., El-Husayni, S., . . . Battinelli, E. M. (2019). Aspirin inhibits platelets from reprogramming breast tumor cells and promoting metastasis. Blood Adv, 3(2), 198-211. doi: 10.1182/bloodadvances.2018026161

Jurasz, P., Alonso-Escolano, D., Radomski, M. W. (2004). Platelet–cancer interactions: mechanisms and pharmacology of tumour cell-induced platelet aggregation. Br J Pharmacol, 143(7), 819-826. doi: 10.1038/sj.bjp.0706013

Karreman, M. A., Mercier, L., Schieber, N. L., Solecki, G., Allio, G., Winkler, F., . . . Schwab, Y. (2016). Fast and precise targeting of single tumor cells in vivo by multimodal correlative microscopy. J Cell Sci, 129(2), 444-456. doi: 10.1242/jcs.181842

Katagiri, Y., Hayashi, Y., Baba, I., Suzuki, H., Tanoue, K., Yamazaki, H. (1991). Characterization of platelet aggregation induced by the human melanoma cell line HMV-I: roles of heparin, plasma adhesive proteins, and tumor cell membrane proteins. Cancer Res, 51(4), 1286-1293.

Kristiansen, G., Winzer, K. J., Mayordomo, E., Bellach, J., Schluns, K., Denkert, C., . . . Dietel, M. (2003). CD24 expression is a new prognostic marker in breast cancer. Clin Cancer Res, 9(13), 4906-4913.

Labelle, M., Begum, S., Hynes, R. O. (2011). Direct signaling between platelets and cancer cells induces an epithelial-mesenchymal-like transition and promotes metastasis. Cancer Cell, 20(5), 576-590. doi: 10.1016/j.ccr.2011.09.009

Labelle, M., Begum, S., Hynes, R. O. (2014). Platelets guide the formation of early metastatic niches. Proc Natl Acad Sci U S A, 111(30), E3053-3061. doi: 10.1073/pnas.1411082111

Labelle, M., Hynes, R. O. (2012). The initial hours of metastasis: the importance of cooperative host-tumor cell interactions during hematogenous dissemination. Cancer Discov, 2(12), 1091-1099. doi: 10.1158/2159-8290.CD-12-0329

Lazar, S., Goldfinger, L. E. (2021). Platelets and extracellular vesicles and their cross talk with cancer. Blood, 137(23), 3192-3200. doi: 10.1182/blood.2019004119

Lebozec K., Jandrot-Perrus M. , Avenard G. , Favre-Bulle O., Billiald P.. Design, development and characterization of ACT017, a humanized Fab that blocks platelet's glycoprotein VI function without causing bleeding risks. MAbs. 2017 Aug/Sep; 9(6):945-958

Li, R., Ren, M., Chen, N., Luo, M., Deng, X., Xia, J., . . . Wu, J. (2014). Presence of intratumoral platelets is associated with tumor vessel structure and metastasis. BMC Cancer, 14, 167. doi: 10.1186/1471-2407-14-167

Lucotti, S., Muschel, R. J. (2020). Platelets and Metastasis: New Implications of an Old Interplay. Front Oncol, 10, 1350. doi: 10.3389/fonc.2020.01350

Ma, C., Fu, Q., Diggs, L. P., McVey, J. C., McCallen, J., Wabitsch, S., . . . Greten, T. F. (2022). Platelets control liver tumor growth through P2Y12-dependent CD40L release in NAFLD. Cancer Cell, 40(9), 986-998 e985. doi: 10.1016/j.ccell.2022.08.004

Pierre Henri Mangin, ChaoJun Tang, Catherine Bourdon, Stéphane Loyau, Monique Freund, Béatrice Hechler, Christian Gachet, Martine Jandrot-Perrus. A humanized glycoprotein VI (GPVI) mouse model to assess the antithrombotic efficacies of anti-GPVI agents. J Pharmacol Exp Ther. 2012 Apr;341(1):156-63.

Mammadova-Bach, E., Gil-Pulido, J., Sarukhanyan, E., Burkard, P., Shityakov, S., Schonhart, C., . . . Nieswandt, B. (2020). Platelet glycoprotein VI promotes metastasis through interaction with cancer cell-derived galectin-3. Blood, 135(14), 1146-1160. doi: 10.1182/blood.2019002649

McCarty, O. J., Jadhav, S., Burdick, M. M., Bell, W. R., Konstantopoulos, K. (2002). Fluid shear regulates the kinetics and molecular mechanisms of activation-dependent platelet binding to colon carcinoma cells. Biophys J, 83(2), 836-848. doi: 10.1016/S0006-3495(02)75212-0

Miller, S. P., Sanchez-Avalos, J., Stefanski, T., Zuckerman, L. (1967). Coagulation disorders in cancer. I. Clinical and laboratory studies. Cancer, 20(9), 1452-

1465. doi: 10.1002/1097-0142(196709)20:9<1452::aid-cncr2820200912>3.0.co;2-t
Monroe, D. M., Key, N. S. (2007). The tissue factor-factor VIIa complex: procoagulant activity, regulation, and multitasking. J Thromb Haemost, 5(6), 1097-1105. doi: 10.1111/j.1538-7836.2007.02435.x
Nieswandt, B., Hafner, M., Echtenacher, B., Mannel, D. N. (1999). Lysis of tumor cells by natural killer cells in mice is impeded by platelets. Cancer Res, 59(6), 1295-1300.
Osmani, N., Follain, G., Garcia Leon, M. J., Lefebvre, O., Busnelli, I., Larnicol, A., . . . Goetz, J. G. (2019). Metastatic Tumor Cells Exploit Their Adhesion Repertoire to Counteract Shear Forces during Intravascular Arrest. Cell Rep, 28(10), 2491-2500 e2495. doi: 10.1016/j.celrep.2019.07.102
Osmani, N., Follain, G., Gensbittel, V., Garcia-Leon, M. J., Harlepp, S., Goetz, J. G. (2021). Probing Intravascular Adhesion and Extravasation of Tumor Cells with Microfluidics. Methods Mol Biol, 2294, 111-132. doi: 10.1007/978-1-0716-1350-4_8
Peralta, M., Osmani, N., Goetz, J. G. (2022). Circulating tumor cells: Towards mechanical phenotyping of metastasis. iScience, 25(3), 103969. doi: 10.1016/j.isci.2022.103969
Prandoni, P. (2005). Venous thromboembolism risk and management in women with cancer and thrombophilia. Gend Med, 2 Suppl A, S28-34.
Schlappack, O. K., Baur, M., Steger, G., Dittrich, C., Moser, K. (1988). The clinical course of lung metastases from breast cancer. Klin Wochenschr, 66(17), 790-795. doi: 10.1007/BF01726581
Schumacher, D., Strilic, B., Sivaraj, K. K., Wettschureck, N., Offermanns, S. (2013). Platelet-derived nucleotides promote tumor-cell transendothelial migration and metastasis via P2Y2 receptor. Cancer Cell, 24(1), 130-137. doi: 10.1016/j.ccr.2013.05.008
Schwarz, R. E. (1999). Platelet counts and prognosis of pancreatic cancer. Lancet, 353(9170), 2158-2159. doi: 10.1016/S0140-6736(05)75597-5
Senft, D. (2022). Platelets limit liver tumours. Nat Rev Cancer, 22(11), 608. doi: 10.1038/s41568-022-00520-y
Sood, A. K., Bhatty, R., Kamat, A. A., Landen, C. N., Han, L., Thaker, P. H., . . . Cole, S. W. (2006). Stress hormone-mediated invasion of ovarian cancer cells. Clin Cancer Res, 12(2), 369-375. doi: 10.1158/1078-0432.CCR-05-1698
Stewart, T. J., Abrams, S. I. (2007). Altered immune function during long-term host-tumor interactions can be modulated to retard autochthonous neoplastic growth. J Immunol, 179(5), 2851-2859.
Stoletov, K., Kato, H., Zardouzian, E., Kelber, J., Yang, J., Shattil, S., Klemke, R. (2010). Visualizing extravasation dynamics of metastatic tumor cells. J Cell Sci, 123(Pt 13), 2332-2341. doi: 10.1242/jcs.069443
Stone, R. L., Nick, A. M., McNeish, I. A., Balkwill, F., Han, H. D., Bottsford-Miller, J., . . . Sood, A. K. (2012). Paraneoplastic thrombocytosis in ovarian cancer. N Engl J Med, 366(7), 610-618. doi: 10.1056/NEJMoa1110352
Strassel, C., David, T., Eckly, A., Baas, M. J., Moog, S., Ravanat, C., . . . Lanza, F. (2006). Synthesis of GPIb beta with novel transmembrane and cytoplasmic sequences in a Bernard-Soulier patient resulting in GPIb-defective signaling in CHO cells. J Thromb Haemost, 4(1), 217-228. doi: 10.1111/j.1538-7836.2005.01654.x
Szczerba, B. M., Castro-Giner, F., Vetter, M., Krol, I., Gkountela, S., Landin, J., . . . Aceto, N. (2019). Neutrophils escort circulating tumour cells to enable cell cycle progression. Nature, 566(7745), 553-557. doi: 10.1038/s41586-019-0915-y
Tao, D. L., Tassi Yunga, S., Williams, C. D., McCarty, O. J. T. (2021). Aspirin and antiplatelet treatments in cancer. Blood, 137(23), 3201-3211. doi: 10.1182/blood.2019003977
Valastyan, S., Weinberg, R. A. (2011). Tumor metastasis: molecular insights and evolving paradigms. Cell, 147(2), 275-292. doi: 10.1016/j.cell.2011.09.024
Vismara, M., Zara, M., Negri, S., Canino, J., Canobbio, I., Barbieri, S. S., . . . Guidetti, G. F. (2021). Platelet-derived extracellular vesicles regulate cell cycle progression and cell migration in breast cancer cells. Biochim Biophys Acta Mol Cell Res, 1868(1), 118886. doi: 10.1016/j.bbamcr.2020.118886
Voors-Pette, C., Lebozec, K., Dogterom, P., Jullien, L., Billiald, P., Ferlan, P., . . . Jandrot-Perrus, M. (2019). Safety and Tolerability, Pharmacokinetics, and Pharmacodynamics of ACT017, an Antiplatelet GPVI (Glycoprotein VI) Fab. Arterioscler Thromb Vasc Biol, 39(5), 956-964. doi: 10.1161/ATVBAHA.118.312314
Wang, Y. H., Deng, S. J., Yang, Y. D., Yao, N., Zhao, J. M., Min, G. T., . . . Chen, W. (2017). The pretreatment thrombocytosis may predict prognosis of patients with colorectal cancer: a systematic review and meta-analysis. Biomark Med, 11(2), 195-210. doi: 10.2217/bmm-2016-0214
Wojtukiewicz, M. Z., Sierko, E., Hempel, D., Tucker, S. C., Honn, K. V. (2017). Platelets and cancer angiogenesis nexus. Cancer Metastasis Rev, 36(2), 249-262. doi: 10.1007/s10555-017-9673-1
Wu, Q., Li, J., Zhu, S., Wu, J., Chen, C., Liu, Q., . . . Sun, S. (2017). Breast cancer subtypes predict the preferential site of distant metastases: a SEER based study. Oncotarget, 8(17), 27990-27996. doi: 10.18632/oncotarget.15856

MATERIAL and METHODS

Cell lines.

The mouse breast cancer cell lines 4T1, E0771, AT3, and D2A1, and the mouse melanoma cell line B16F0, were cultured under standard conditions (37°C, 5% CO2) using RPMI or DMEM, respectively, supplemented with 10% FBS and 1% penicillin-streptomycin solution. The human breast cancer MDA-MB-231 and melanoma cell lines A375 and MCF7, we cultured under the same conditions (RMPI and DMEM, respectively). Their viabilities in vitro were assayed before aggregation and SEM assays and in vivo experimental metastasis experiments by an ADAM-MC Automated cell counter (NanoEntek).

Cell line engineering.

For in vivo imaging on zebrafish embryos, 4T1 and B16F10

cells were engineered to express a Lifeactin-tdTomato fusion protein. Briefly, the Life-tdTomato DNA fragment derived from the Addgene plasmid tdTomato-Lifeact-7 (number 54528) was inserted in the pLSFFV-Ires-Puromycin lentivirus vector to generate the pLSFFV-LifeActin-tdTomato-Ires-Puromycin lentivirus vector. Lentivirus particles production and transduction procedures have been already described in (Hyenne et al., 2019) For confocal imaging of single arrested TCs in mice lungs, 4T1 or B16F10 cells were labeled in vitro with CellTrace Yellow (Thermo Fischer) according to manufactured instructions. For in vivo imaging in mice, regular firefly luciferase or red-shifted firefly luciferase (Bioware® Brite B16F10-Red-FLuc, Perkin Elmer) was used. B16F10 cells expressing red-shifted luciferase were purchased from Perkin Elmer. 4T1 luciferase-expressing cells were a kind gift from Corinne Laplace-Builhé (Institut Gustave Roussy Paris). To generate a luciferase-expressing breast cancer AT3 cell line (Stewart Abrams, 2007), we engineered it to express the red-shifted luciferase protein using the RediFect Red-Fluc Lentiviral Particles from Perkin-Elmer. To avoid immune rejection in immunocompetent C5BL6/J recipients, an in vivo-derived AT3 cell line was established from lung metastases derived from a tail vein-injected mouse. Briefly, mouse lungs containing AT3-RedFLuc metastasis were collected on Day 18 post-injection and chopped into 1 mm3 pieces with a scalpel. The pieces were resuspended in 4000µl of dissociation buffer (Miltenyi Biotec Neural Tissue Dissociation Kit (P) 130-092-628) in the presence of 100µl of collagenase solution (Sigma-Aldrich C9891) at 100mg/ml together with 400µl of DNaseI at 1mg/ml under gentle mixing at 37°C during 10 min. 50µl of enzyme P was added and further incubated for 5 min. 60µl of enzyme A was added with an additional incubation period of 5 min. The suspension was then ground on a Corning cell strainer of 40µm (reference 431750) over a 50ml falcon tube using a 2.5ml syringe rubber plunger. Four ml of full cell medium were added to the filtrated solution and cells were then collected by centrifugation, 5 min, 400g at room temperature. The pellet was resuspended in RPMI medium containing 10% FCS, 1% PS, 1% Gentamicin, 5µg/ml of Fungizone, and puromycin at 1µg/ml in a T75 flask. After a few days of puromycin selection, the cell line was considered established and called AT3-RedFluc-LM1. To ensure the absence of immune rejection on recipients a second round of in vivo derivation was performed, thus generating the AT3-RedFluc-LM2 cell line which was used in our experiments.

Platelets isolation.

For obtaining human platelets suspensions, the blood was collected in the presence of 1/10 volume of citric acid-citrate-dextrose (ACD) pH 6.5 and 1 U/ml apyrase, from healthy volunteers with informed consent, who had not taken any drugs known to affect platelet function for at least 14 days before the study. Platelet-rich plasma was prepared by centrifugation at 250g for 10 min at room temperature and collection of the supernatant. Washed platelets were prepared as described previously (Heinrich et al. 1985). Briefly, blood was centrifuged at 250g for 16 minutes at 37C. Supernatant (cPRP) was collected and centrifuged at 2200g (time of centrifugation depends on volume). Platelet pellet was resuspended in pre-warmed (37C) Tyrode-Albumin buffer (TA) (0.35% HAS, anhydrous D-glucose, NaCl 137 mM, KCl 2.7 mM, NaHCO3 12 mM, NaH2PO4 0.36 mM, HEPES 5mM, 2 mM CaCl2+ 1 mM MgCl2, pH 7.35, 295 mOsm/L) containing 10U/L of Heparin and 0.5 mM of PGI2. Platelet suspension was incubated for 10 minutes at 37C. Heparin and PGI2 were added again to the tubes, centrifuged at 1900g for 8 minutes and the supernatant was discharged. Pellet was re-suspended and centrifuged again in TA buffer with 0.02U/ml of apyrase. Pellet was re-suspended in TA buffer with 0.02U/ml of apyrase at a platelet concentration of 300 x 103 platelets/l. The quality of the platelet suspension was routinely tested by ADP 5mM and Thrombin (0.1U/mL) aggregation assay in the presence of fibrinogen. For obtaining mouse platelet suspensions, the blood was collected by an aortic puncture after intraperitoneal injection of anesthesia (ketamine 100mg/kg, xylazine 20mg/kg). Anesthetized animals were placed on heating pads at 38 C for dissection. By the use of a sterile tissue pad, abdominal organs were side displaced to show the thoracic portion of the aortic artery. A preloaded jeringe with citric acid 0,15% was used to collect the blood by punction at the level of the separation of the aortic artery into the two iliac arteries. Around 700-800 ml of blood was collected per mouse. Mice were sacrificed while anesthetized by cervical dislocation.

Zebrafish handling and intravascular injection of tumor cells.

Tg(fli1a:eGFP) Zebrafish (Danio rerio) embryos from a Tubingen background used in the experiments were kindly provided by the group of F. Peri from EMBL (Heidelberg, Germany) and further grown and bred in our in-house Zebrafish facility. Embryos were maintained in Danieau 0.3X medium (17,4 mM NaCl, 0,2 mM KCl, 0,1 mM MgSO4, 0,2 mM Ca(NO3)2) buffered with HEPES 0,15 mM (pH = 7.6), supplemented with 200 µM of 1-Phenyl-2-thiourea (Sigma-Aldrich) to inhibit the melanogenesis, as previously described (Goetz et al., 2014). Forty-eight-hour post-fertilization (hpf) Tg(Fli1a:eGFP) embryos were mounted in a 0.8% low melting point agarose pad containing 650µM of tricaine (ethyl-3-aminobenzoatemethanesulfonate) to immobilize the embryos. D2A1 LifeAct-RFP cells were injected with a Nanoject microinjector 2 (Drummond) and microforged glass capillaries (25 to 30 µm inner diameter) filled with mineral oil (Sigma). 23nL of a cell suspension at 100000 cells per ml was injected in the duct of Cuvier of the embryos under the M205 FA stereomicroscope (Leica), as previously described (Follain et al., 2018).

Mice.

Male WT C5BL6/J immunocompetent mice from 8 to 16 weeks were used for the B16F10 melanoma cell model, while female WT immunocompetent Balb/c mice were used for the 4T1 breast cancer model. All were purchased from Charles River Labs. Animals were housed in pathogen free condi-

tions. Mice received standard chow and sterile tap water ad libitum. Appropriate enrichment (sterile pulp paper and coarsely litter) was provided. Physical condition of mice was monitored daily. A protocol approved for early euthanasia of terminally sick animals was in place. All animal procedures were performed in accordance with institutional guidelines and approval, under the APAFIS authorization 14741-2018041816337540. C5BL6/J immunocompetent mice deficient for the platelet receptor GPVI (GPVI-/-), and bearing the human form (hGPVI) were generated as previously described (Mangin P.H. et al. 2012).

Platelet and GPVI receptor depletion and pharmacological blockage.
Severe thrombocytopenia was induced by intravenous (i.v.) injection of 50µg of in-house-produced αGPIb antibody (Strassel et al., 2006) or IgG isotype control per mouse (IgG, RAM.6, 2 mg/kg). Injections were delivered at precise time points to differently affect the metastatic cascade, meaning 24 hours prior TCs injection, 3dpi, 7dpi and/or 10dpi. To specifically deplete GPVI receptor in mouse platelets, 100µg of JAQ1 mAb (Emfret) was injected i.v. per mouse. Control animals were injected with 100µg rat IgG isotype control (Emfret). For the delivery of anti-human GPVI antibody Glenzocimab, due to its short half-life in the mouse circulation, an Azlet osmotic pump (model 2001) was implanted subcutaneously (s.c.) on the dorsal side, to deliver the antibody for 7 days, at a rate of 1µl/hours at a concentration of 20mg/ml.

Platelet Counts.
Murine whole blood was collected into EDTA (6 mM) after severing the mouse tail. The platelet count and size were determined in a Scil Vet abc automatic cell counter (Scil Animal Care Company, Holtzheim, France) set to murine parameters. The platelet count on human platelet suspensions (cPRP and/or washed platelets) was assessed in an automatic platelet counter.

Experimental pulmonary metastasis assay and bioluminescent imagings.
Subconfluent 4T1 and B16F10 cells expressing regular luciferase (Photinus pyralis) or red-shifted version, respectively, were washed with PBS (Gibco), detached using a 0.25% trypsin-0.02% EDTA solution (Gibco), washed in media containing 10% fetal calf serum, resuspended in serum-free media, filtered through a 40 µm mesh (filcon) and kept on ice until injection. Viability was determined by trypan blue exclusion and was always more than 85% prior injection. Cells 1.5x 105 in 100 µl of serum-free media were injected per mouse through the lateral tail vein by using a 25-gauge needle. In vivo imaging of mice lungs was immediately performed after tumour cells inoculation to stablish initial lung seeding. Subsequent imaging points at 0.5, 1, 2, 4 and 24h, and 1, 3, 7, 10 and 14 days after TCs injection were monitored. To do so, 5 min after intraperitoneal injection of D-luciferin solution (150mg/kg) to the isofluorane-anesthetized (Isoflo, Zeotis) mouse, the ventral bioluminescence image of mice lungs was acquired with an IVIS Lumina III (Perkin Elmer) imaging system and then analysed using the Living Image software (Perkin Elmer). The rate of total light emission of the lung metastatic area was calculated and expressed as numbers of photons emitted per second (p/s).

Light transmission aggregometry (LTA).
TC-induced platelet aggregation (TCIPA) was analyzed by LTA. Human citrated platelet rich plasma (cPRP) and washed platelets were isolated from citrated blood of human donors according to the approval of the local ethics committee. Murine citrated platelet rich plasma (cPRP) was obtained by aortic puncture after centrifugation of the whole blood during 5 min at 100g. Serum free media or TA buffer were used as control. Platelet aggregation was measured at 37°C by a standard turbidimetric method in an APACT 4004 aggregometer (ELITech Group, Puteaux, France). For human platelet aggregations the following procedures were used. To 200l of washed platelets at a final platelet concentration of 3x105/l, or citrate platelet rich plasma (cPRP), 50µl of TCs suspended in TA buffer or serum free culture media, respectively, were added. For the aggregation of washed platelets, 50 µl of TCs suspension (final concentration up to 3x106/ml) were added to 200µl washed platelets (final concentration 3x105/ml). Platelets suspensions were stirred at 1,100 rpm. Control samples were activated by the addition of 5µM ADP in the presence of TCs, human fibrinogen (0.05 mg/mL) or human collagen (concentration) in a final volume of 300µL. Prior aggregation, TCs were washed twice in RPMI-1640 medium without serum + 0.1% BSA + 2mM CaCl2 + 1mM MgCl2, or in TA buffer. Platelet aggregation was evaluated by comparing the amplitudes of the aggregation curves generated with APACT LPC software.

Scanning Electron Microscopy.
Cells were washed in serum free media (cPRP) or TA buffer (washed platelets) prior incubation with platelet suspensions. PEG (Polyethylene glycol) blocked beads were used as a control. TCs and platelet mixes resulting after LTA assay were immediately fixed in 2x fixative solution (4% paraformaldehyde, 5% glutaraldehyde in standard 0.1M Sodium Cacodylate buffer, NaCac). TCs and platelet aggregates were sedimented O/N at 4ºC. Supernatants were removed and pellets gently resuspended in NaCac Buffer. For sample dehydration 1,1,1,3,3,3-hexamethyldizilazane (HDMS, Merck, Millipore) was used. Cells were mounted onto 25,4mm EM Aluminum Mounts for AMRAY (EMS, Hatfield) by using Leit-C conductive carbon cement (CCC, Plano GmbH, Germany). Platinum metallization of the sample was performed under vacuum by using a Cressington Sputter Coater 208HR coupled to a Pfeiffer Vacuum (Germany). Image acquisition was performed at high-resolution (10-15kV) and 6000-10000x magnification on a PhenomWorld SEM desktop microscope (Phenom-World B.V, The Netherlands).

Electron microscopy sample preparation and image acquisition.
Correlative Light and Electron Microscopy was performed as

previously described (Goetz et al., 2014). To describe ultrastructural characteristics of CTC-bound platelets interacting with the ZF endothelium, chosen ZF embryos were chemically fixed with 2.5% glutaraldehyde and 2% paraformaldehyde in 0.1M NaCac buffer (pH 7.4). The sample was kept in fixative for 48hr at 4°C and washed 3 times with 0.1M NaCac buffer, pH7.4, followed by a second fixation with 0,05% malachite green, 2.5% glutaraldehyde in 0.1M NaCac buffer, pH7.4 during 25 min in an ice bath. The sample then was post-fixed for 45 min in 1% OsO4 in 0.1M NaCac buffer, pH7.4 in a fume hood in an ice bath and washed 2 times with in 0.1M NaCac, (the buffer was also kept in an ice bath to avoid thermal changes). Then the specimen was incubated in 1% aqueous tannic acid solution for 25 min in an ice bath and finally washed 5 times with distilled water (DW). The zebrafish sample was dehydrated with serial ethanol solutions (25%, 50%, 70% 95% and 100%) and dry acetone at RT for 10 min. Subsequently the sample was incubated in a serial resin-acetone solution (1:3; 1:1; 3:1). Further, the sample was incubated in 100% Epon resin 3 times 1h at RT. The sample was allowed to polymerize in an oven at 60°C for 48h. The resin block was trimmed by ultramicrotomy. After targeting region of interest (ROI), 90 nm thin sections were collected and placed in slot Formvar cupper grids. The TEM data set was acquired with a Hitachi 7500 TEM, with 80 kV beam voltage, and the 8-bit images were obtained with a Hamamatsu camera C4742-51-12NR. The collected images were processed for segmentation using an open-source software ImageJ; AMIRA and IMARIS as follows: a) single images were stitched in a bigger composed image and combined into a 3D-stack; b) The combined 3D-stack was aligned and the contrast adjusted, by ImageJ. C) The segmentation of objects of interest, (arrested tumor cells, platelets) and, 3D Volume reconstruction, by AMIRA and IMARIS.

Tissue histology and immunohistochemistry.

Mice were sacrificed under isofluorane anesthesia and lidocaine analgesia (5mg/kg) at 15mpi, 2hpi and 15dpi. Lungs were resected, washed and fixed O/N in 4% paraformaldehyde/phosphate buffered saline (PBS) solution (EMS). Left lung lobes were then treated for paraffin inclusion, while the right lung lobes were treated for Optimal Cutting Temperature (OCT) inclusion (Tissue freezing media, Leica). Briefly, O/N fixed lungs were subjected to dehydration on serial grades of ethanol and a final xylene/toluene bath. Dehydated tissue was then paraffin embedded in an automated Leica inclusion machine. Cryosections of 20µm (single cell analyses and segmentation) or 10µm (regular IF analyses) paraffin sections were mounted on poly-lysine-coated slides (SuperFrost UltraPlus, Thermo Fisher Scientific). In the case of paraffin-embedded samples, tissue antigens were retrieved by boiling in sodium citrate solution (10 mM, pH 6.0, Sigma). For blocking unspecific antibody binding sites, samples were incubated for 1 h in blocking solution (3% bovine serum albumin, 20 mM MgCl2, 0.3% Tween 20, 5% fetal bovine serum in PBS). Background and nonspecific staining was determined by incubating tissue samples in the absence of primary antibody. Proliferation index within metastatic foci was calculated by the staining with a rabbit anti-mouse Ki67 antibody (clone SP6, Thermo Fisher). For CD45 staining, a mouse biotinilated anti-mouse CD45 antibody (clone 30-F11, Biolegend) was used. Prior to the addition of secondary antibody, tissue endogenous biotin was quenched with Avidin/Biotin blocking solution (Vector Laboratories). Development of the biotinilated antibody signal was done by 1 h incubation with the Avidin/Biotin-HRP complex (Elite Vectastain ABComplex Kit, Vector Laboratories) following 1 h incubation with Streptavidin-647 (BioLegend). For metastases delimitation cytokeratin (mouse anti-mouse cytokeratin pan-mixture, ascites, Sigma) and luciferase (rabbit anti-firefly luciferase, ab21176, Abcam) expression was used in 4T1 and B16F10 metastatic foci, respectively. For the staining of mouse platelets an in-house generated anti-GPIb antibody (Rat anti-mouse GPIb (CD42b) RAM.1) was used. For the detection of primary antibody signals, the following Alexa-labeled (Invitrogen) secondary antibodies were used: goat anti-rabbit (H+L) Highly Cross-Adsorbed Alexa-555, goat anti-mouse (H+L) Highly Cross-Adsorbed Alexa-555, goat anti-rat (H+L) Highly Cross-Adsorbed Alexa-488 or 647. In all cases, nuclei were stained with DAPI (Thermo Fisher Scientific) and slides mounted with Fluoromount-G (SouthernBiotech).

Laser Scanning Confocal Microscopy (LSCP).

For immunohistochemical analyses images were acquired using a Leica TCS SP8 laser scan confocal microscope using a 63×Plan-Apochromat [oil (NA 1.4)] magnification. For 3D segmentation of cells and platelet aggregates, z-stacks (1AU) of single cells or clusters were acquired in 12-bit color depth and non-saturating settings. For in vivo imaging of TCs circulation and arrest on the Tg(fli1a:eGFP) zebrafish embryos a Leica TCS SP8 microscope equipped using a 20x/1.0 W-Plan-Apochromat objective (Leica) was used.

Image processing and analysis.

Metastatic foci number and size was obtained by image processing on ImageJ software. Briefly, macroscopic 8-bit lung (B16F10-seeded) images (MacOS 15.4, iPhone8) with identical zooming and size (100 x 100 px) were loaded on imageJ. Automatic threshold of the images yield a binary mask that were analyzed by the "analyze particles" plugin. Circularity was set between 0.2-1.0 to exclude lung edge shadows. Pixel size bellow 15px was considered as noise. Platelet aggregates and cell volumes arrested intravascularly in mice lungs were obtained by segmentation in AMIRA Visage 6 after confocal acquisition of Z-stacks covering the whole cell-aggregate volume. Brightness and contrast was equally adjusted in control and treated samples on ImageJ and/or Adobe Photoshop CS4 software. Metastatic foci counting was performed in Image J software using the Analyze Particles plugin.

Statistics.

Statistical analysis was performed with GraphPad Prism 5.4 or later version Software. The normal distribution of the data was tested using the Shapiro–Wilk normality test. When comparing two groups, a Mann-Whitney analysis were used,

for more then 2 groups a Kruskal-Wallis test ffollowed by the original FDR method of Benjamini and Hochberg post test was used. For kinetics a Two-way ANOVA followed by Original FDR method of Benjamini and Hochberg post test was used. $p<0.05$, *; $p<0.01$, ** . $p<0.001$, ***; $p<0.0001$, ****. In all cases, the α-level was set at 0.05. Data in graphs are presented as mean ± Standard Deviation.

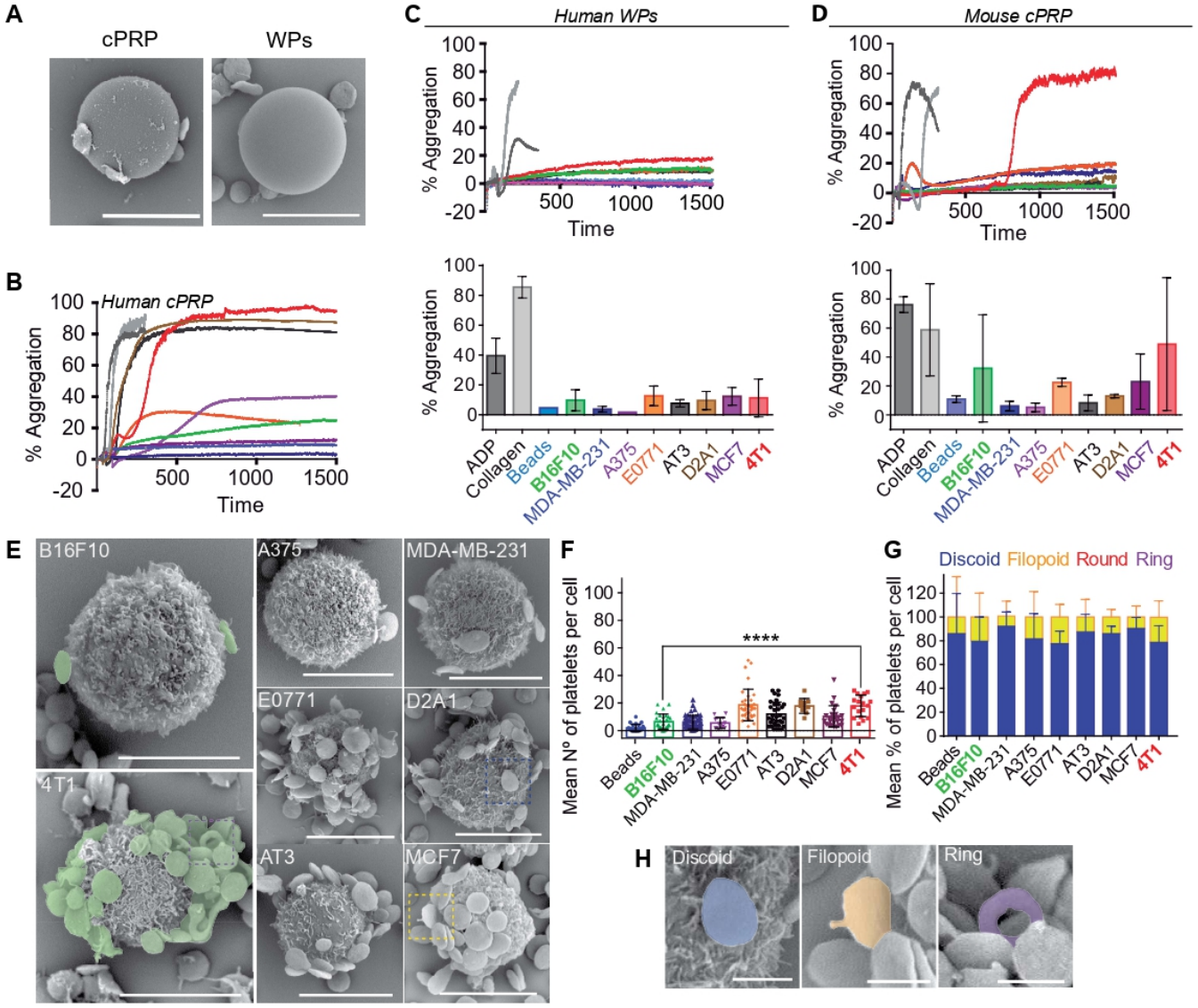

Fig.S1 6. SEM controls and representative aggregation curves (A) SEM images of PEG-treated 10µm polystyrene beads interacting with mouse platelets contained within mouse citrated platelet rich plasma (cPRP) or with human washed platelets (WPs). (B) Representative platelet aggregation curves obtained with human cPRP for each of the TCs studied and ADP and collagen are used as positive controls, while beads are used as negative control. (C) Platelet aggregation efficiency (%) of the different TCs studied in a classic TCIPA assay using human WPs (bottom) and their corresponding representative aggregation curves (top). Representative data from 2 to 3 independent aggregation experiments shown as mean +/- SD. (D) Platelet aggregation efficiency (%) of the different TCs studied in a classic TCIPA assay using mouse cPRP (bottom) and their corresponding representative aggregation curves (top). No significant differences between 4T1 and B16F10 aggregation efficiency was observed due to the high variability of the assay. Representative data from 2 to 4 independent aggregation experiments shown as mean +-/ SD. (E) SEM images of TCs interacting with human washed platelets (WPs), thus in the absence of plasma proteins. 4T1 and B16F10 cells are highlighted, as they still show the most different platelet binding profiles (high versus low, respectively). (F) Platelet binding profiles quantification graph of (F). Kluskal-Wallis with false discovery rate post-test, +-SD, from 2 to 4 independent experiments. (G) Relative number (%) of TC-bound platelets and their respective activation states, mostly discoid (resting) and filopoid (low activation). Round shapes were not observed in the absence of plasma proteins. Ring-shaped platelets of unknown function were also observed in an almost undetectable frequency. Representative data from a total of 10 to 40 images per cell line from 2 to 3 independent experiments represented as mean +/- SD. (H) SEM images details of TC-bound platelets at different activation states.

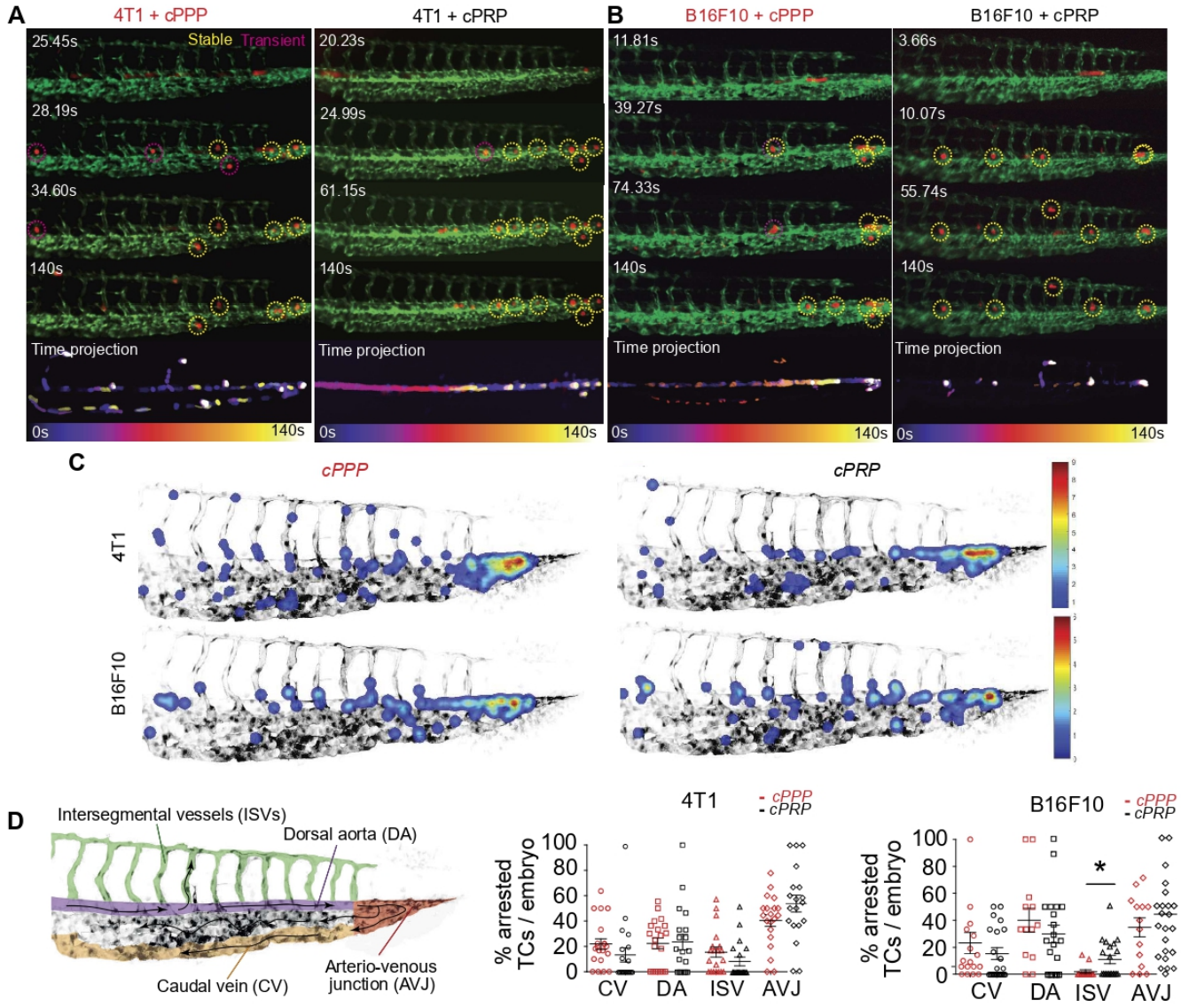

Fig.S2 7. TCs interaction with platelets enhances their intravascular adhesion to the endothelial wall in a cell type-specific manner (A) Live video microscopy time-frames and time projection of 4T1 CTCs circulation and arrest within the ZF caudal plexus in the presence (cPRP) and the absence (cPPP) of human platelets. Yellow circles highlight 4T1 cells that circulate and arrest and stay in a sole position during the 5 minutes of the live imaging (stable arrest). Magenta circles highlight B16F10 cells that circulate and/or arrest briefly (transient arrest). 20 embryos were analysed from 4 independent experiments. (B) Same as (A) but with B16F10, 15 embryos analyzed from 4 independent experiments. (C) Analysis by heat mapping of 4T1 and B16F10 CTCs arrest position in the presence (cPRP) or absence (cPPP) of human platelets at 5mpi. Images show TCs heatmapping in Matlab. (D) On the left, areas of the circulatory system are analysed. On the right, manual counting of CTC number per ZF by vessel type (CV: caudal veins; DA: dorsal aorta; ISV: intersegmental vessels; AVJ: arterio-venous junction) in 4T1 and B16F10 models respectively. For the 4T1 model, 20 embryos were from a total of 4 independent experiments. For the B16F10 model, 15 embryos from 4 independent experiments. Data are shown as mean +/- SD.

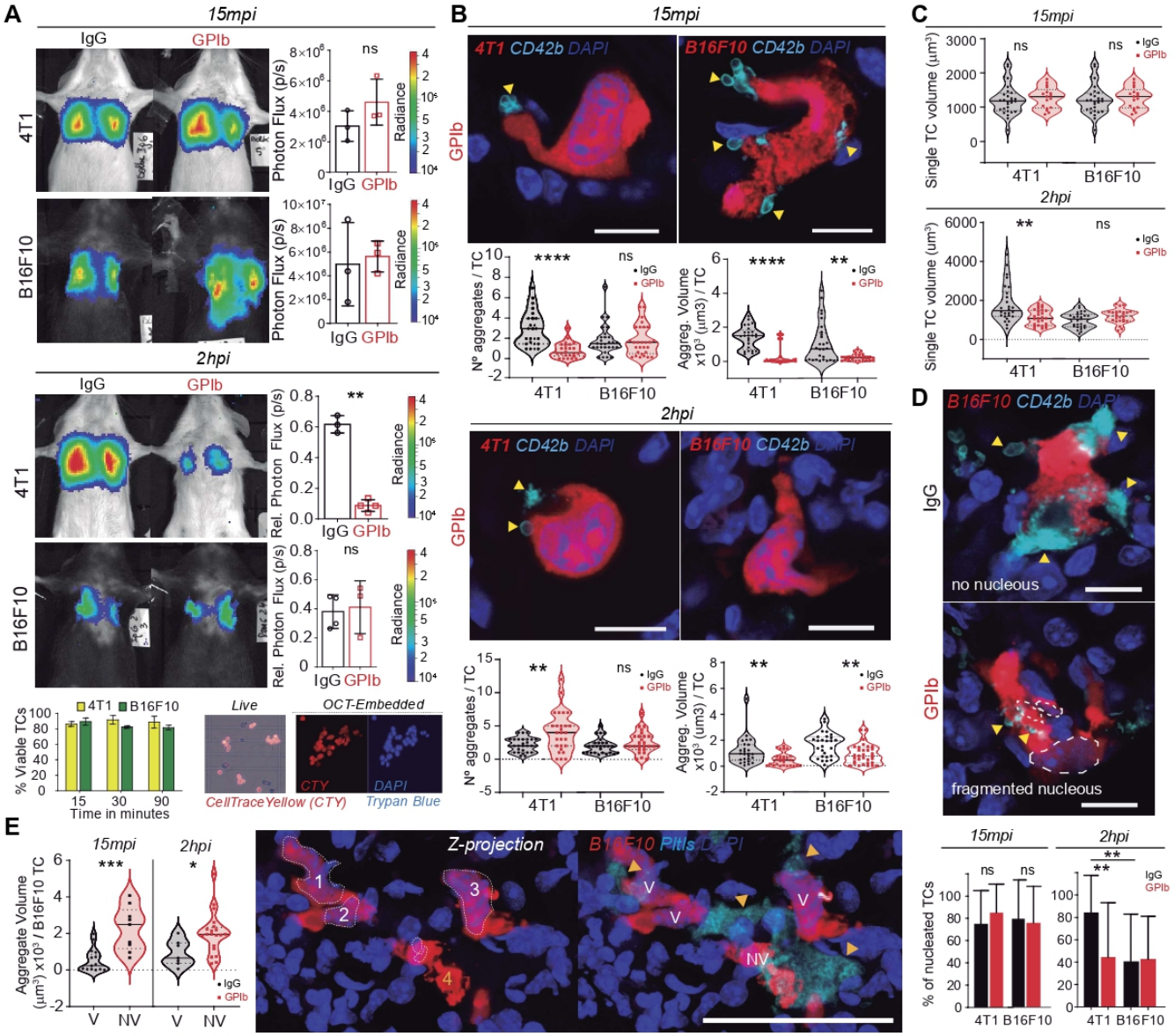

Fig.S3 8. TCs' active or passive interaction with platelets enhances their intravascular survival (A) Representative images and time point comparisons of total lung bioluminescence in normal versus TCP mice in the 4T1 (up) and B16F10 (down) TCs models used for IF analyses of TC intravascular arrest. Two cohorts of mice were used, the first was sacrificed at 15mpi (upper panel) and the second at 2hpi (lower panel). Data are represented as mean +/- SD of 6 mice from 1experiment, Mann-Whitney analysis. Bottom left part, relative in vitro viabilities of 4T1 and B16F10 cells, up to 90min. Bottom right, live imaging, and PFA-fixed / OCT-embedded 4T1 TCs labeled with CellTrace Yellow. (B) Representative AMIRA segmentation images of single TCs arrested intravascularly in the mouse lungs after 15 minutes post-injection (upper panel) and 2hpi (lower panel). Scale: 10m. Violin plots represent the number of aggregates per TC and the volume of aggregates per TC calculated using AMIRA segmentation of confocal images. (C) Violin plots depicting TCs volumes were calculated in AMIRA to obtain an estimation of cell viability, which were compared between TC models and control versus TCP mice. Same analysis as in (B). (D) Representative images of lung-arrested non-viable B16F10 cells, as shown by the absence or fragmented nucleus. Scale: 10m. Bar graphs (bottom) show the frequency (%) of viable B16F10 cells at 15mpi and 2hpi calculated by nuclear integrity. Mann-Whitney analysis from one experiment with a minimum of 25 single TC images per group per cell model, for each time point. Data are shown as mean +/- SD. (E) Representative confocal images of intravascular B16F10 clusters at 2hpi depicting viable cells co-opted together with non-viable cells and large platelet aggregates. Scale: 10m. Left: Violin plots showing the volume of platelet aggregates around viable (V) and non-viable (NV) B16F10 at 15 mpi and 2phi. Same analysis as in (B).

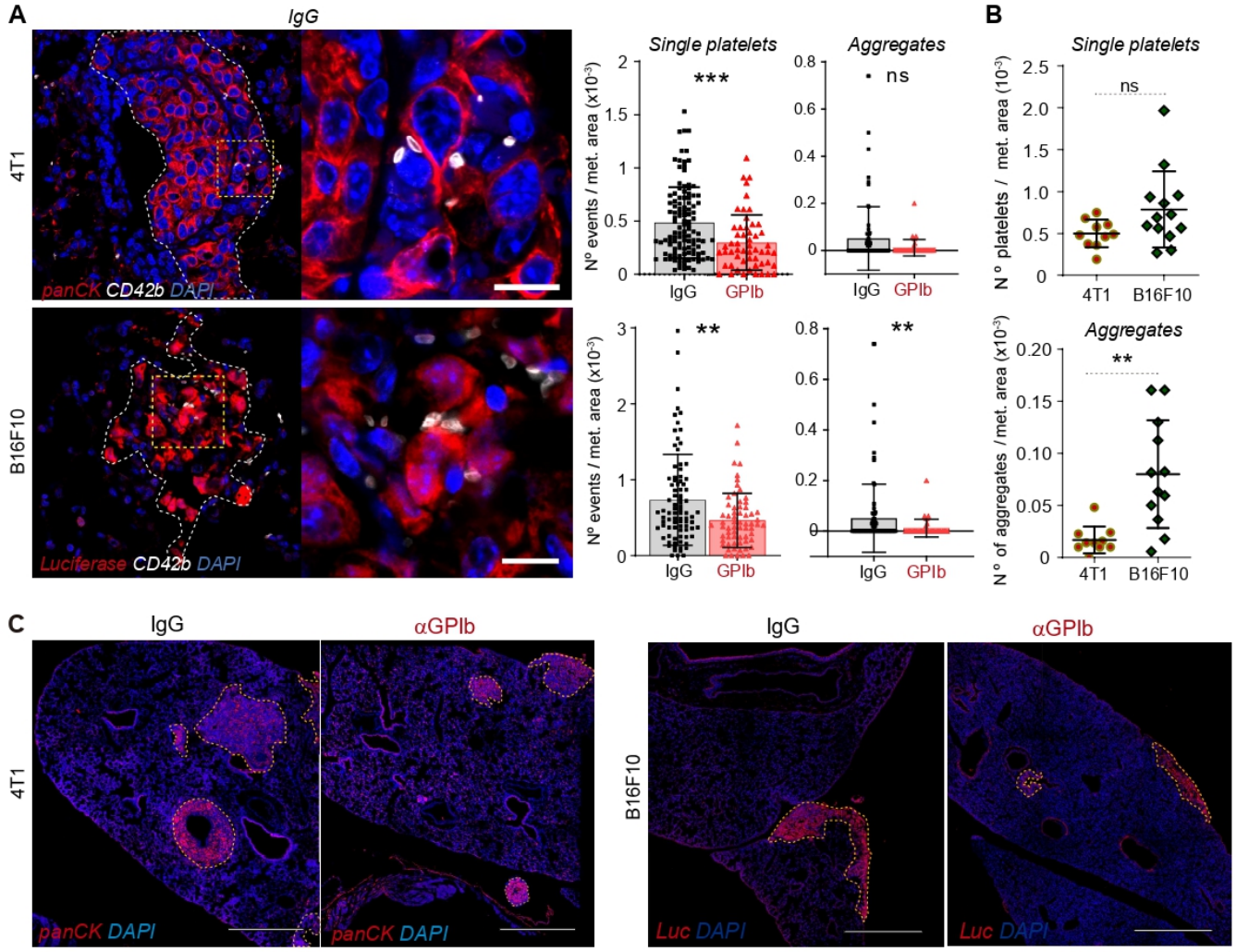

Fig.S4 9. (A) Left: Representative confocal images of mouse lung metastatic foci from 4T1 (top) and B16F10 (bottom) cells at 14dpi stained for the platelet market CD42b. Scale = 50µm. Right: Bar graphs showing the number of single platelet events (3 platelets, left) and number of platelet aggregates (> 3 platelets together, right) per metastatic area, defined by α-pancytokeratin (4T1, top) or α-luciferase staining (B16F10, bottom). (B) Bar graphs comparing the number of platelets (top) and platelet aggregates (bottom) per metastatic area found in control animals of both 4T1 and B16F10 models. Data are represented as the mean +/- SD of 10 images or more per mice, from a total of 8 to 12 mice, from 3 independent experiments, Mann-Whitney analysis. (C) Low magnification confocal images of lung metastases defined by pancytokeratin (4T1) or luciferase (B16F10) stainings at day 14 post-injection. Panels show images of control, short-term TCP mouse models injected with both 4T1 (left) and B16F10 (right) TCs. Scale bar: 100µm.

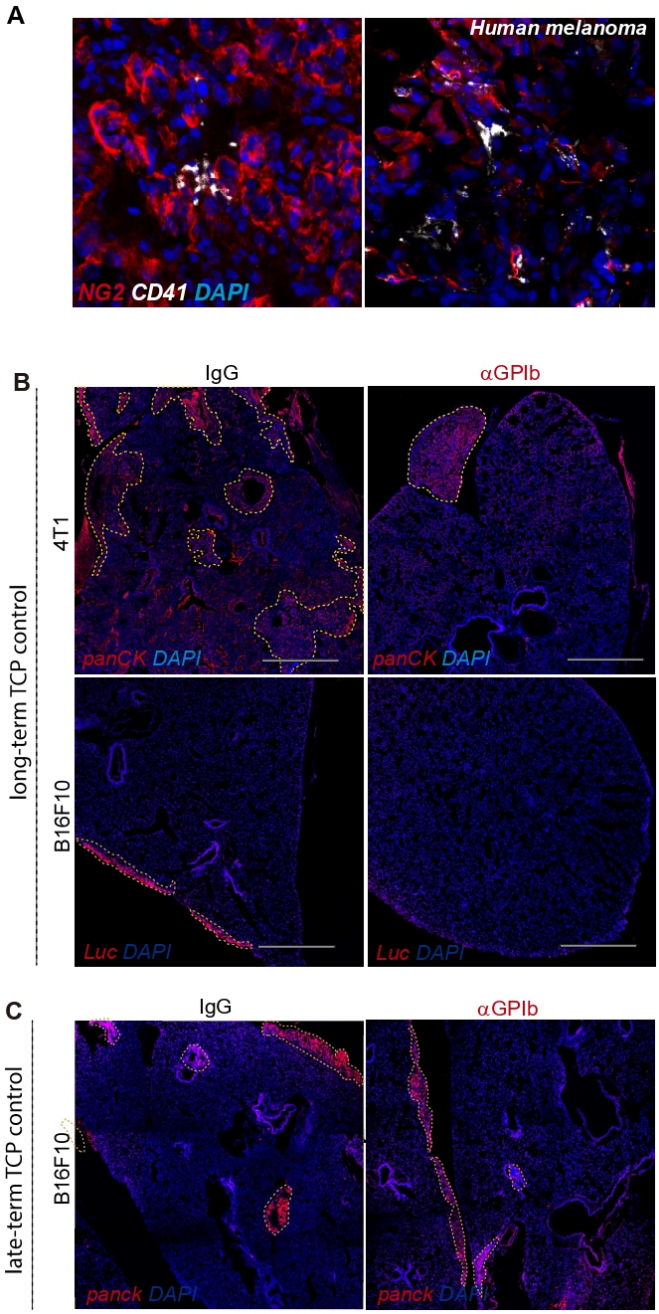

Fig.S5 10. Platelets are present within lateTCP mouse and human lung metastatic foci (A) Representative confocal images of human biopsies from melanoma metastases revealing the presence of intrametastatic platelets and platelet aggregates after specific staining with α-CD41 and α-NG2 markers. (B) Low magnification confocal images of lung metastases defined by panCK (4T1) or luciferase (B16F10) stainings at day 14 post-injection. Panels show images of control, long-term TCP mouse models injected with both 4T1 (top) and B16F10 (bottom) TCs. Scale bar: 100µm. (C) As in (B), but for late-term TCP and only for B16F10) TCs.

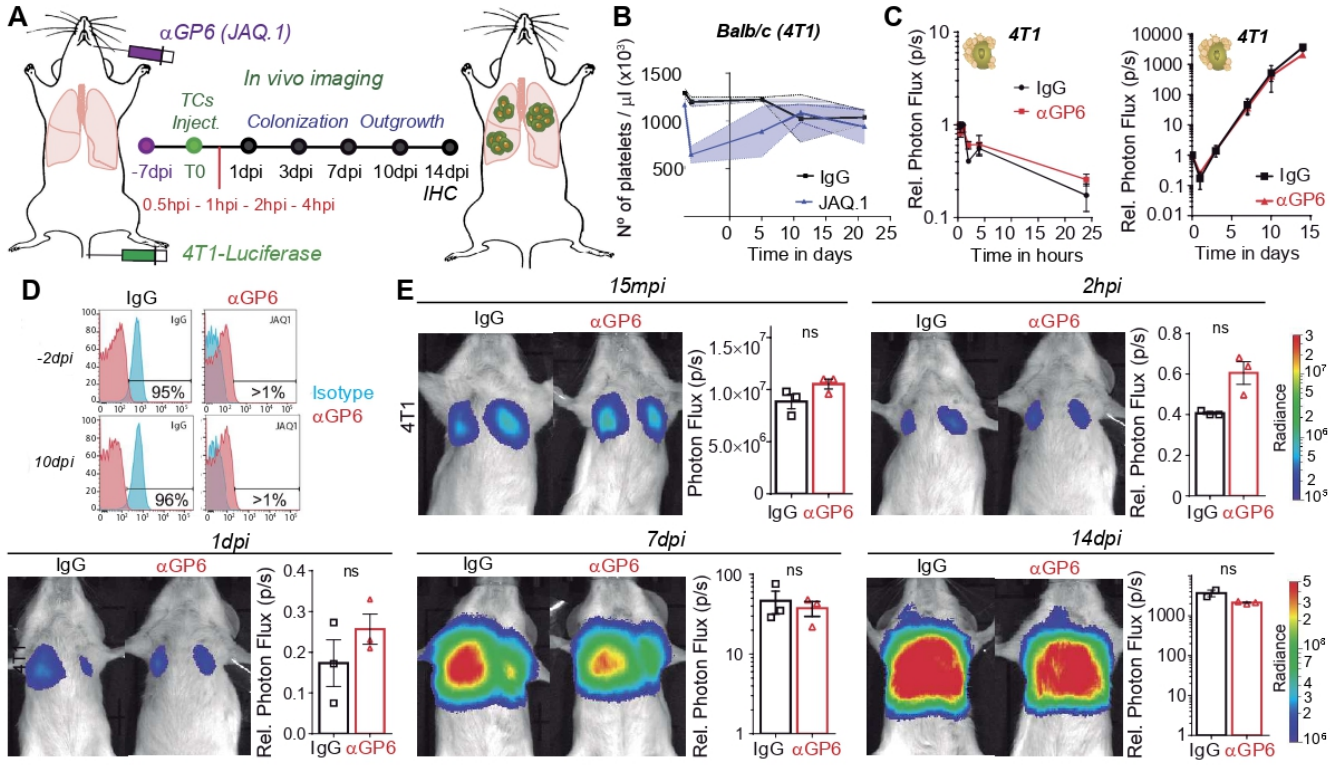

Fig.S6 11. Pharmacologic blockage of the GPVI receptor does not affect lung seeding and metastatic potential of high-binding profile TCs (A) Infographics showing the experimental setting to study the role of platelet receptor GPVI in the early and late events of the metastatic cascade (14 days) by pharmacological intervention. 4T1 TCs are injected intravenously in normal or α-GPVI-treated mice (one week before) with two I.V. shoots of the GPVI-depleting antibody JAQ.1. Lung seeding and metastatic outgrowth is followed by in vivo bioluminescence during 14 days. (B) Platelets counts in normal vs JAQ.1-treated animals. Despite GPVI depletion, mice show normal platelet counts after 10 days post-injection. (C) Bioluminescence kinetics of 4T1-luc TCs lung seeding (left) and outgrowth (right) in normal and α-GPVI-depleted mice. Two-way Anova with false discovery rate post-test, mean +/- SEM, 1 independent experiments of n=3. (D) Specific depletion of GPVI from platelets was assessed by flow cytometry. (E) Representative images and time point (15mpi to 14dpi) comparisons of total lung bioluminescence in normal versus GPVI-depleted animals. Data are represented as mean +/- SEM of 3 mice per group from 1 experiment, Mann-Whitney analysis.

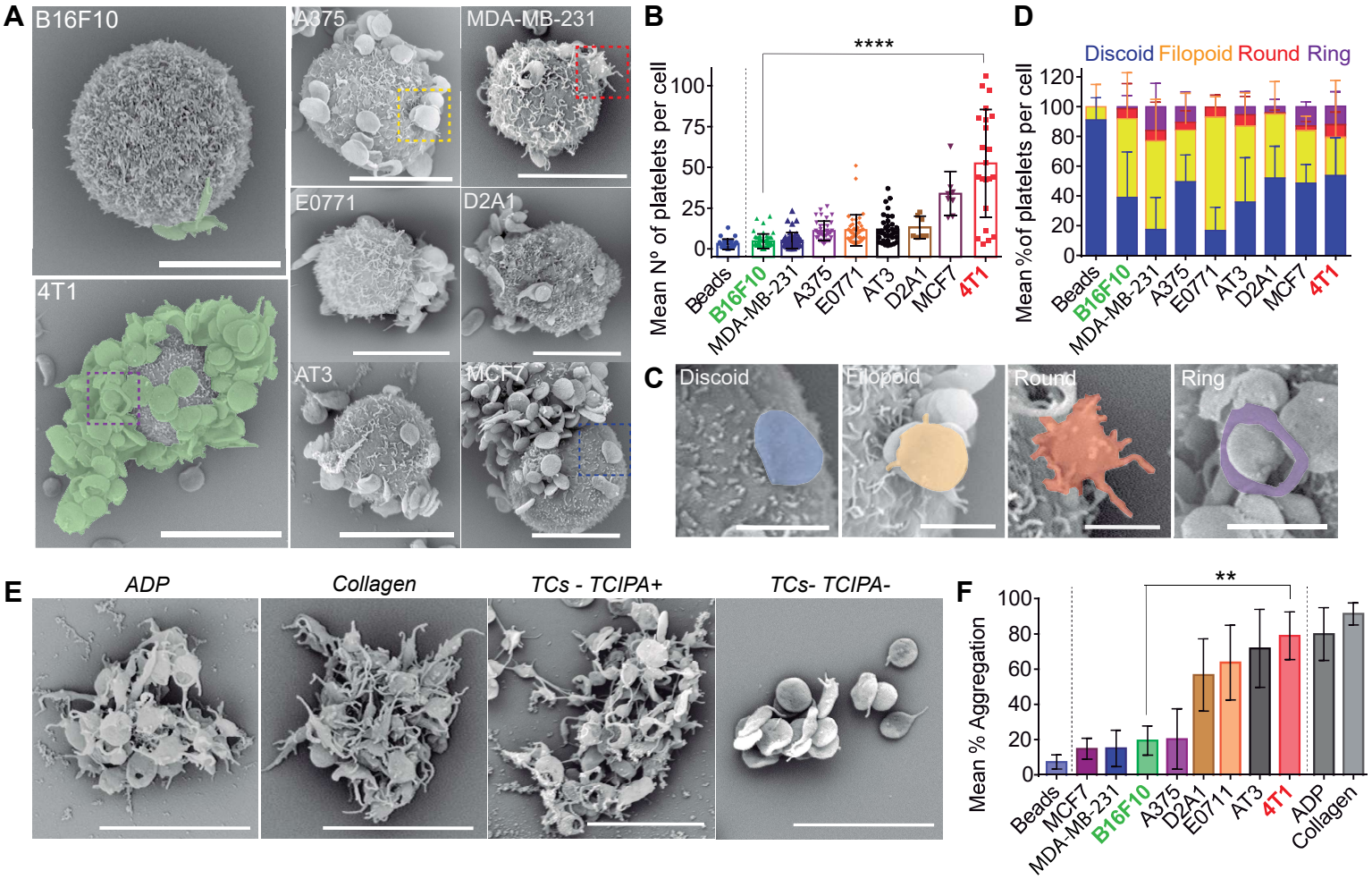

Figure 1. Garcia-Leon *et al.*

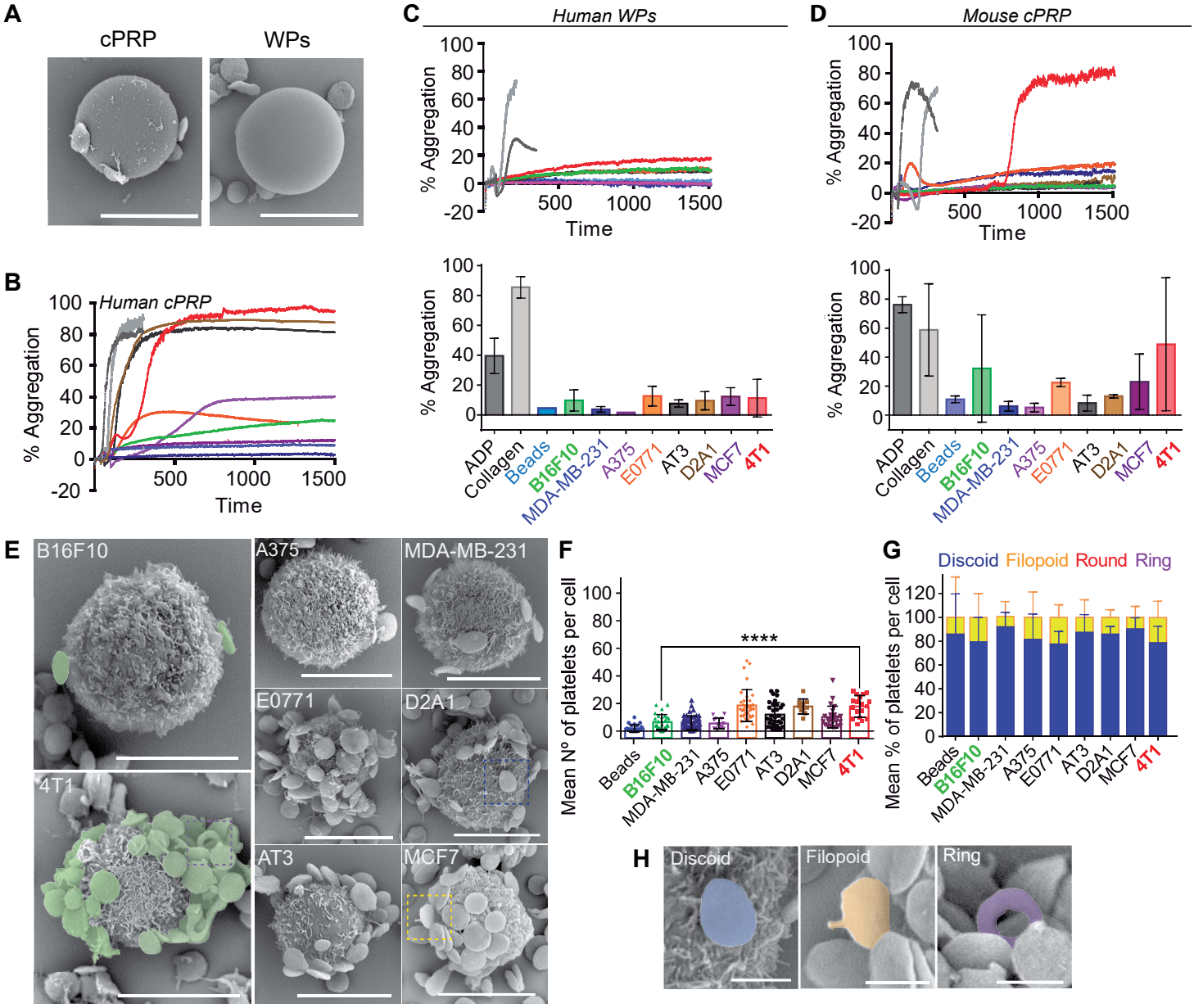

Supplementary Figure 1, related to Figure 1.
Garcia-Leon *et al.*

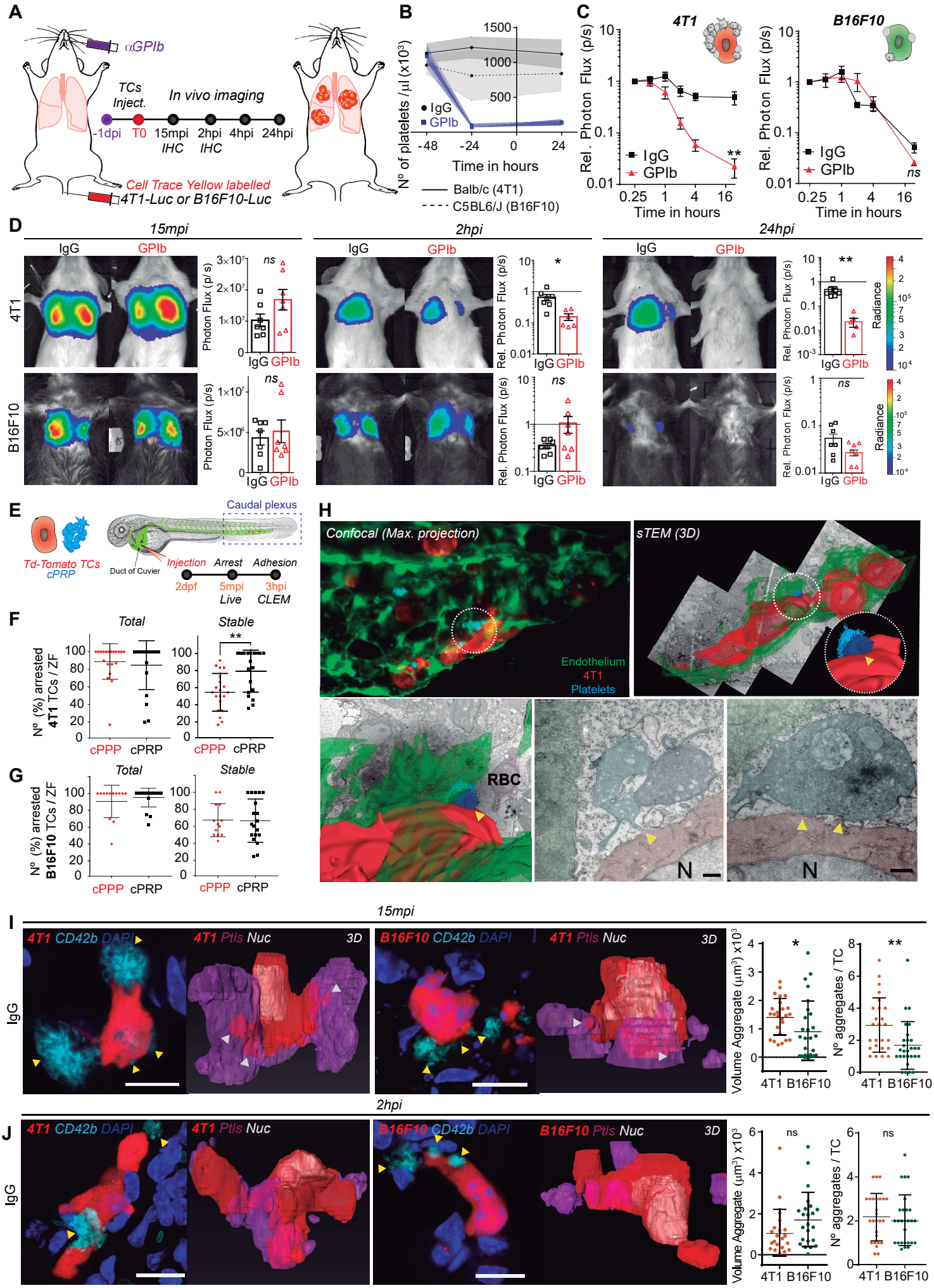

Figure 2. Garcia-Leon M.J. *et al.*

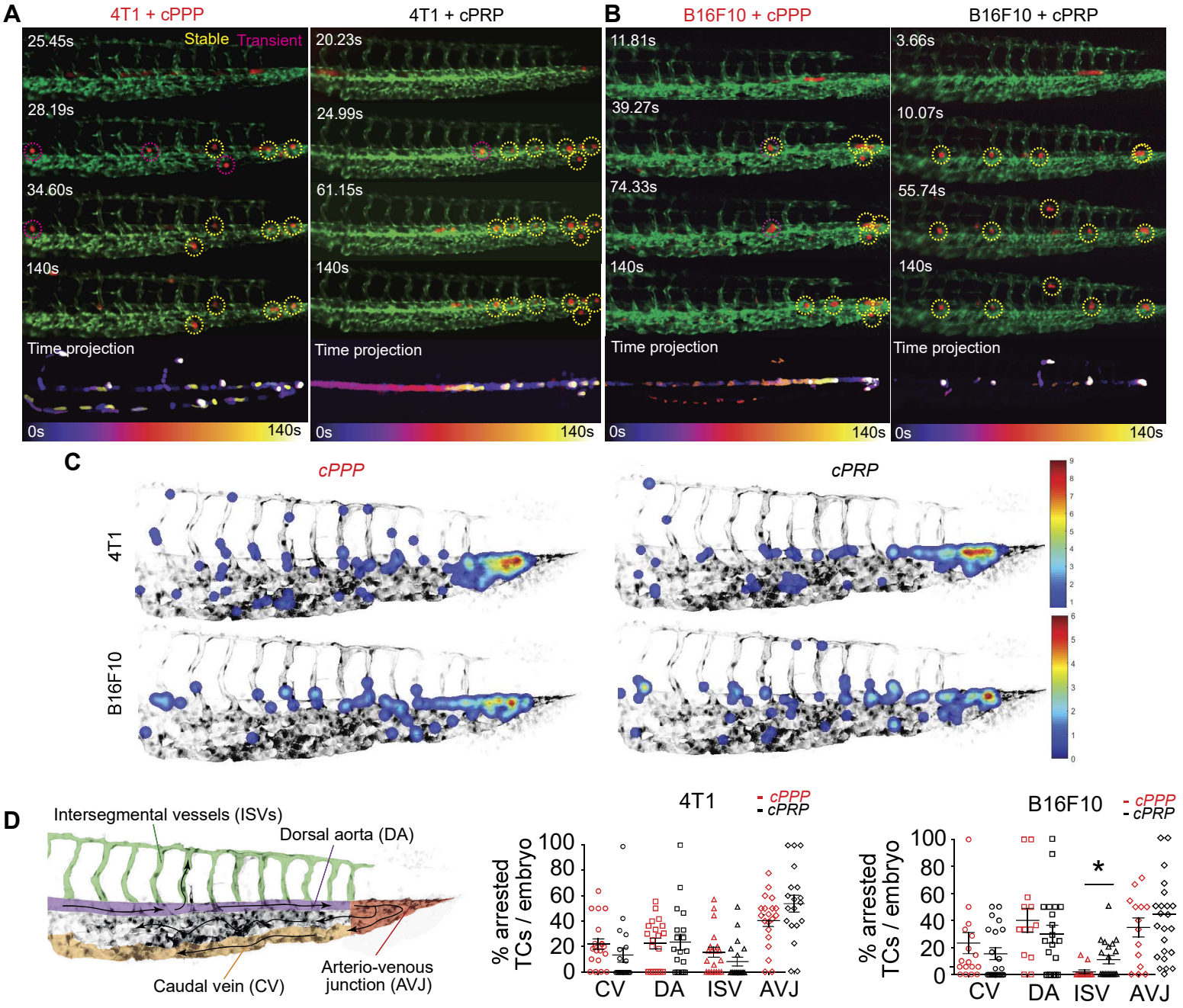

Supplementary Figure 2, related to Figure 2
Garcia-Leon M.J. *et al.*

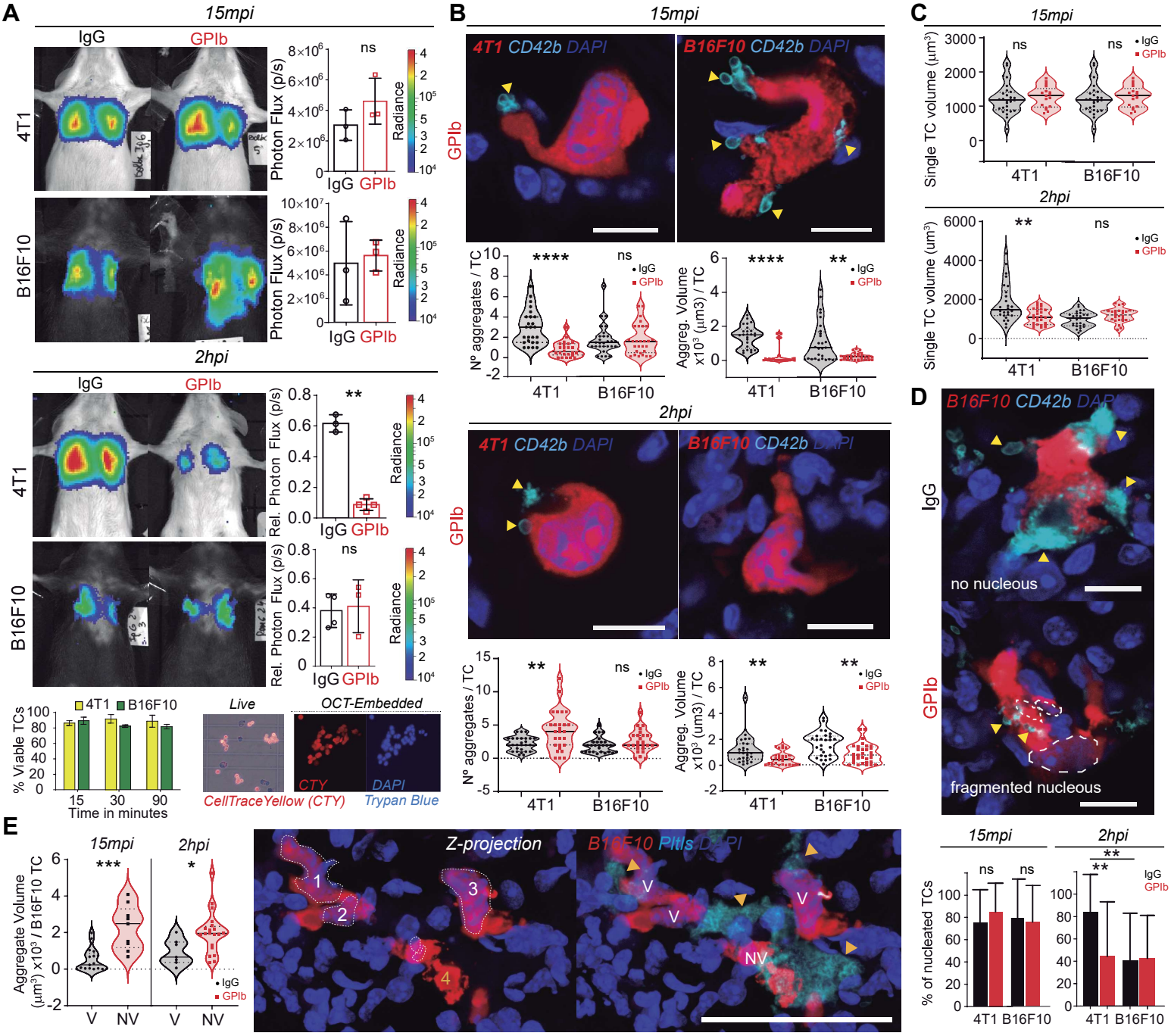

Supplementary Figure 3, related to Figure 2.
Garcia-Leon M.J. *et al.*

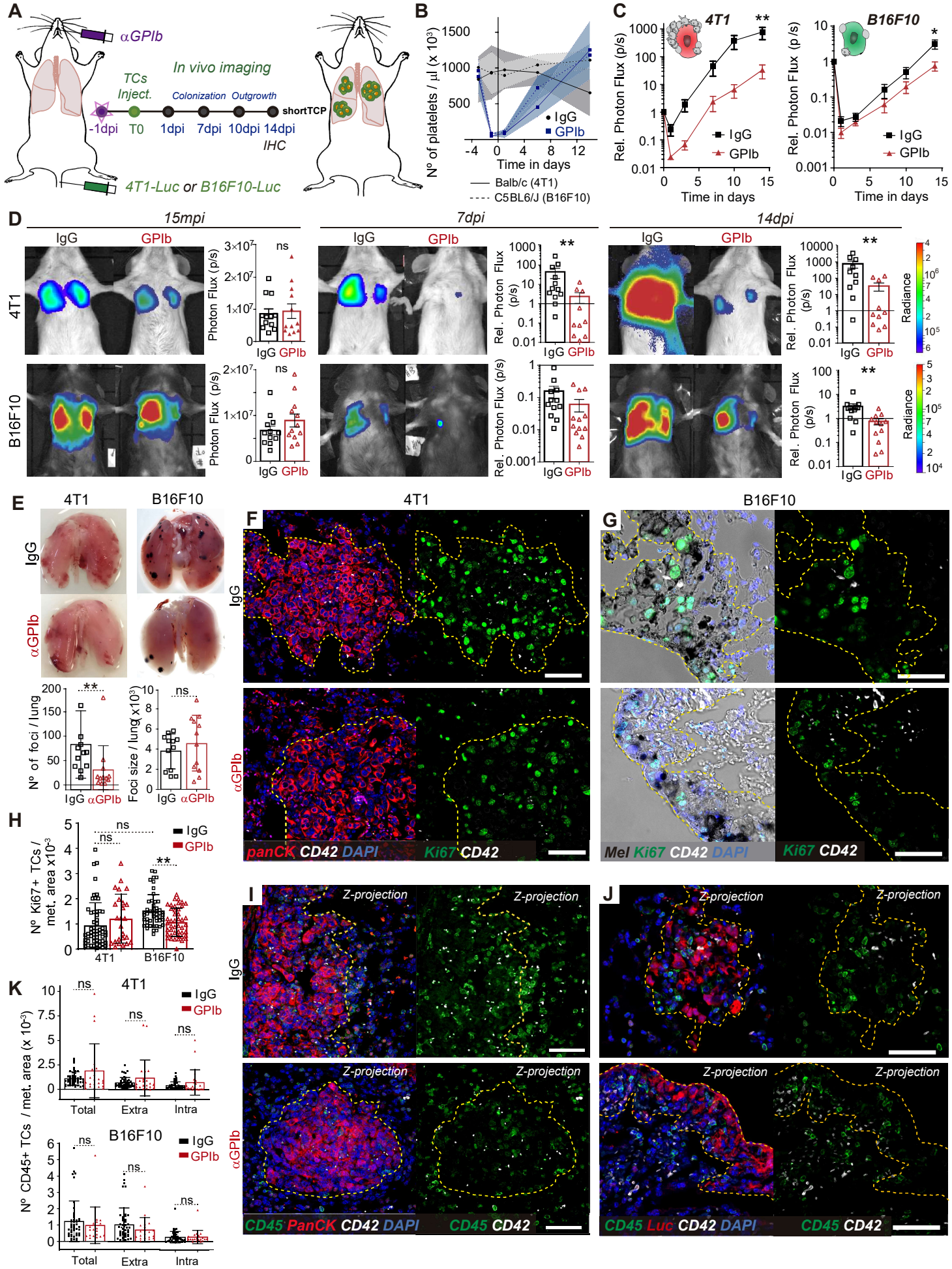

Figure 3. Garcia-Leon *et al.*

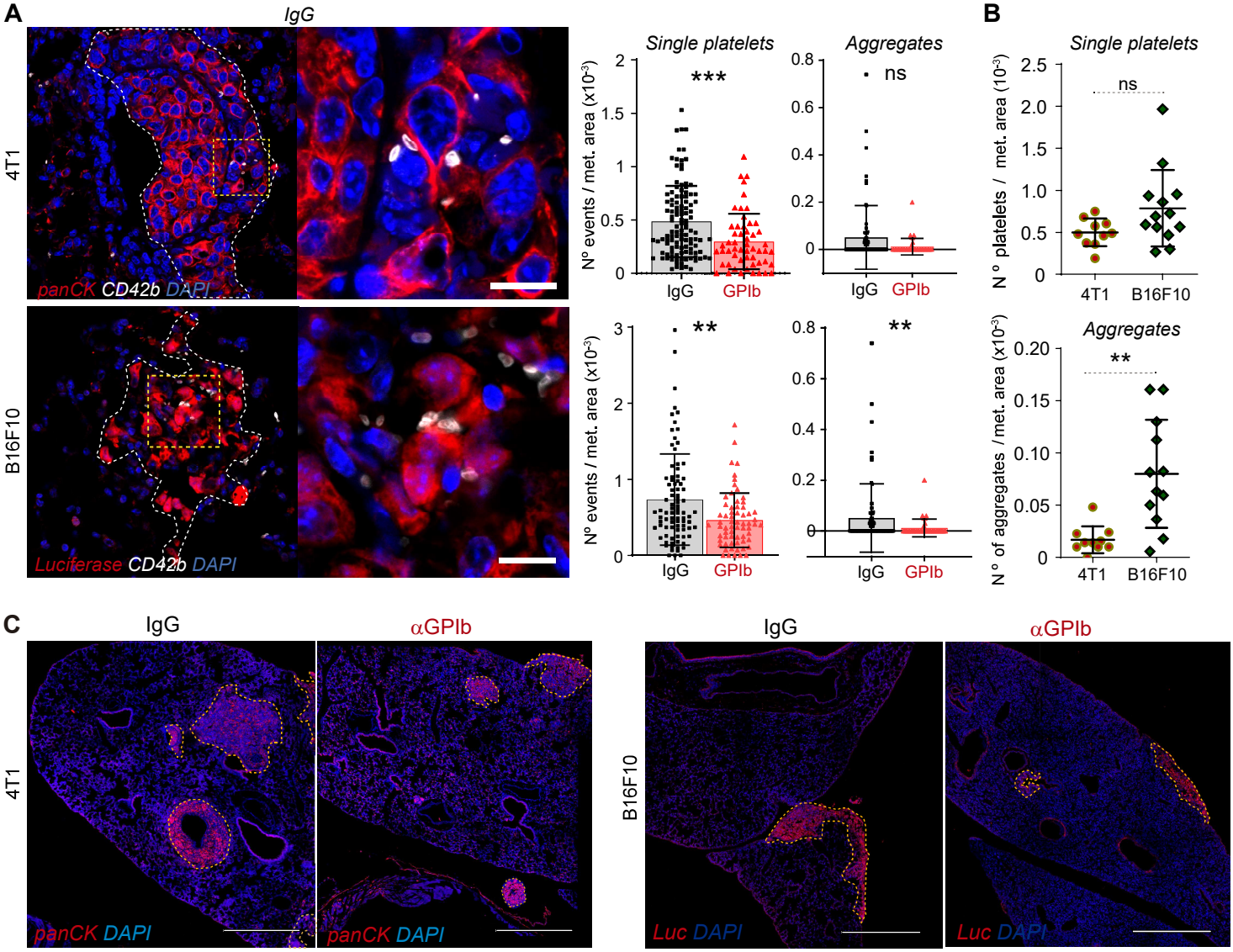

Supplementary Figure 4, related to Figure 3.
Garcia-Leon M.J. *et al.*

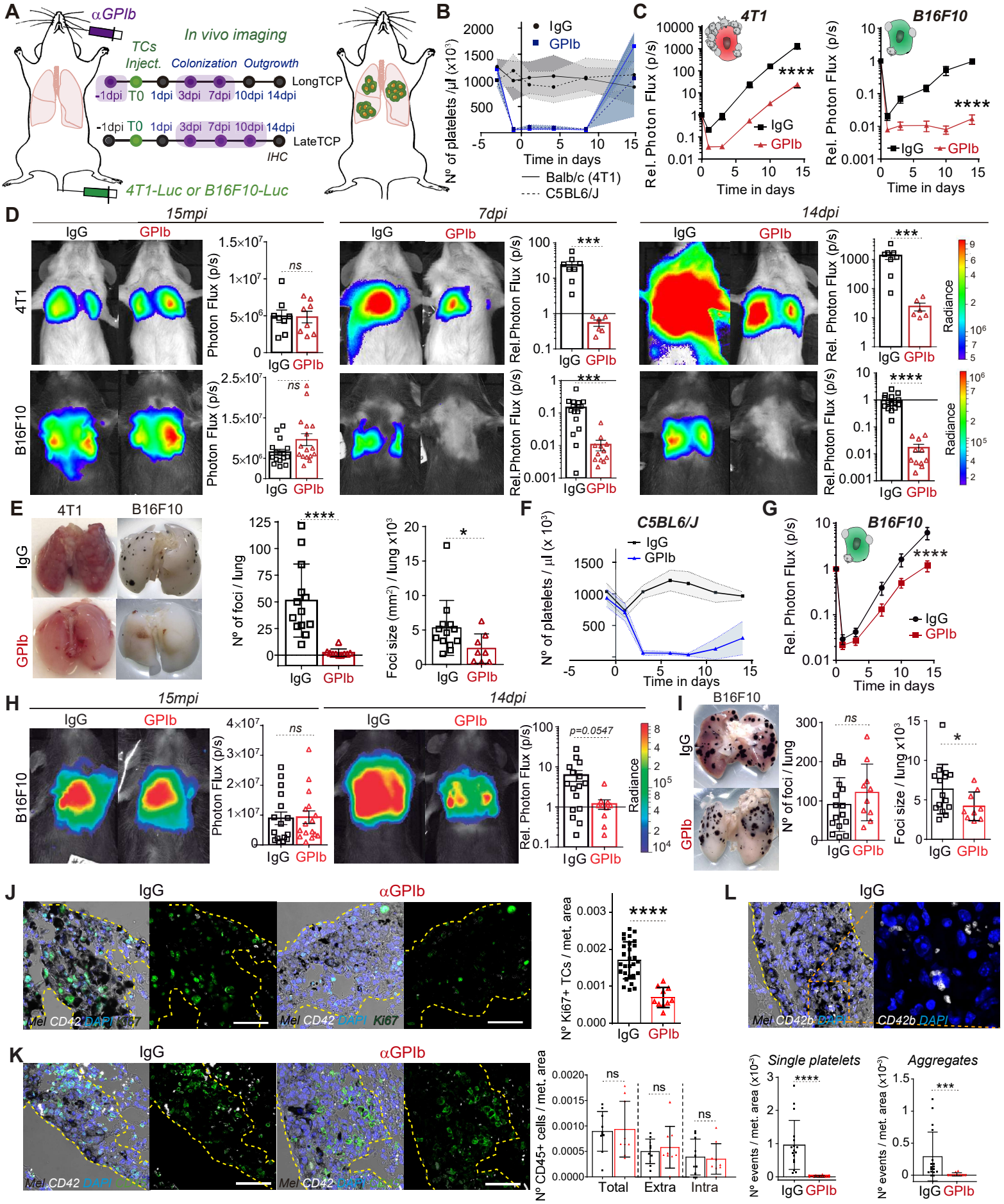

Figure 4. Garcia-Leon *et al.*

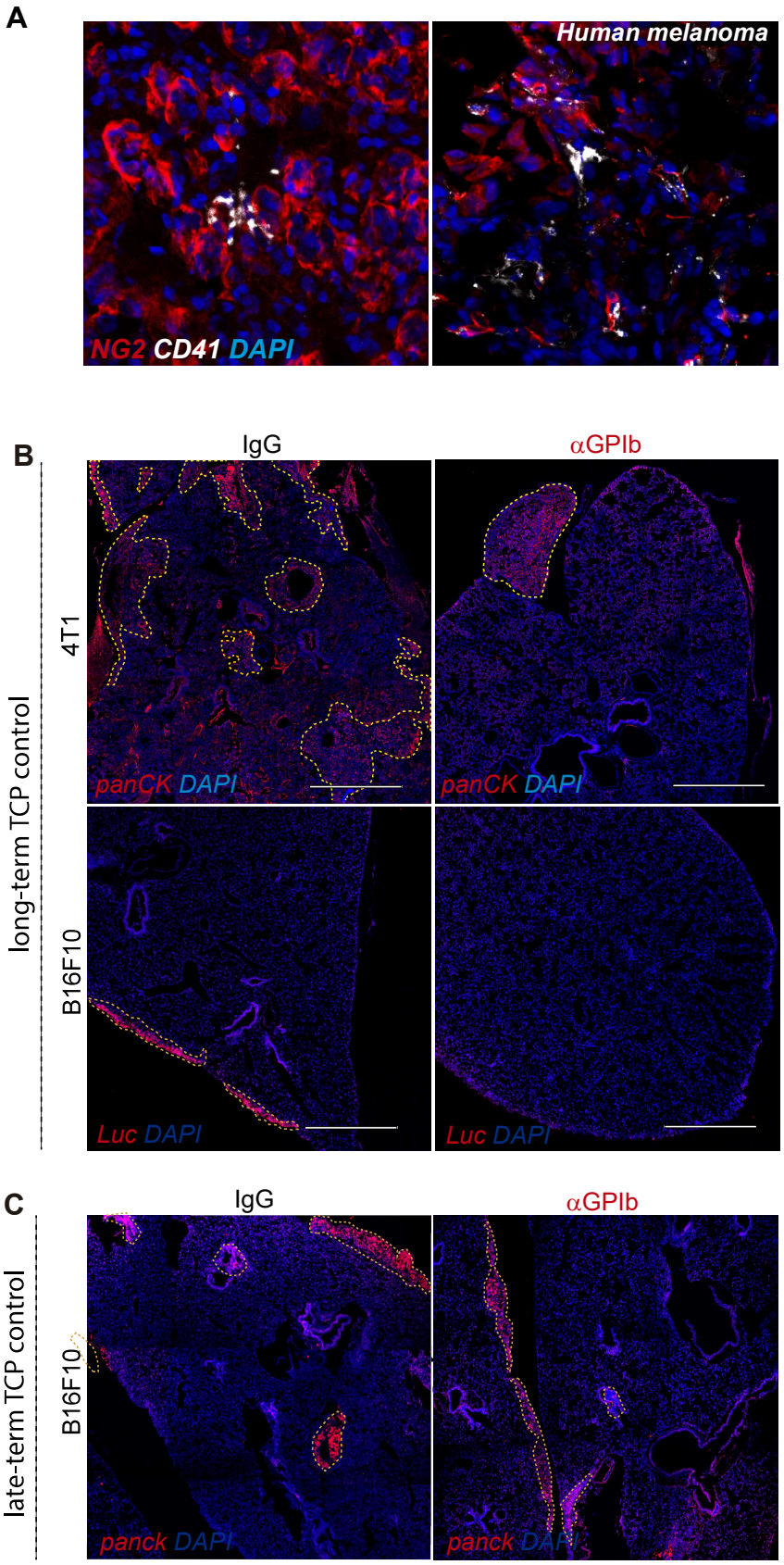

Supplementary Figure 5, related to Figure 4.
Garcia-Leon *et al.*

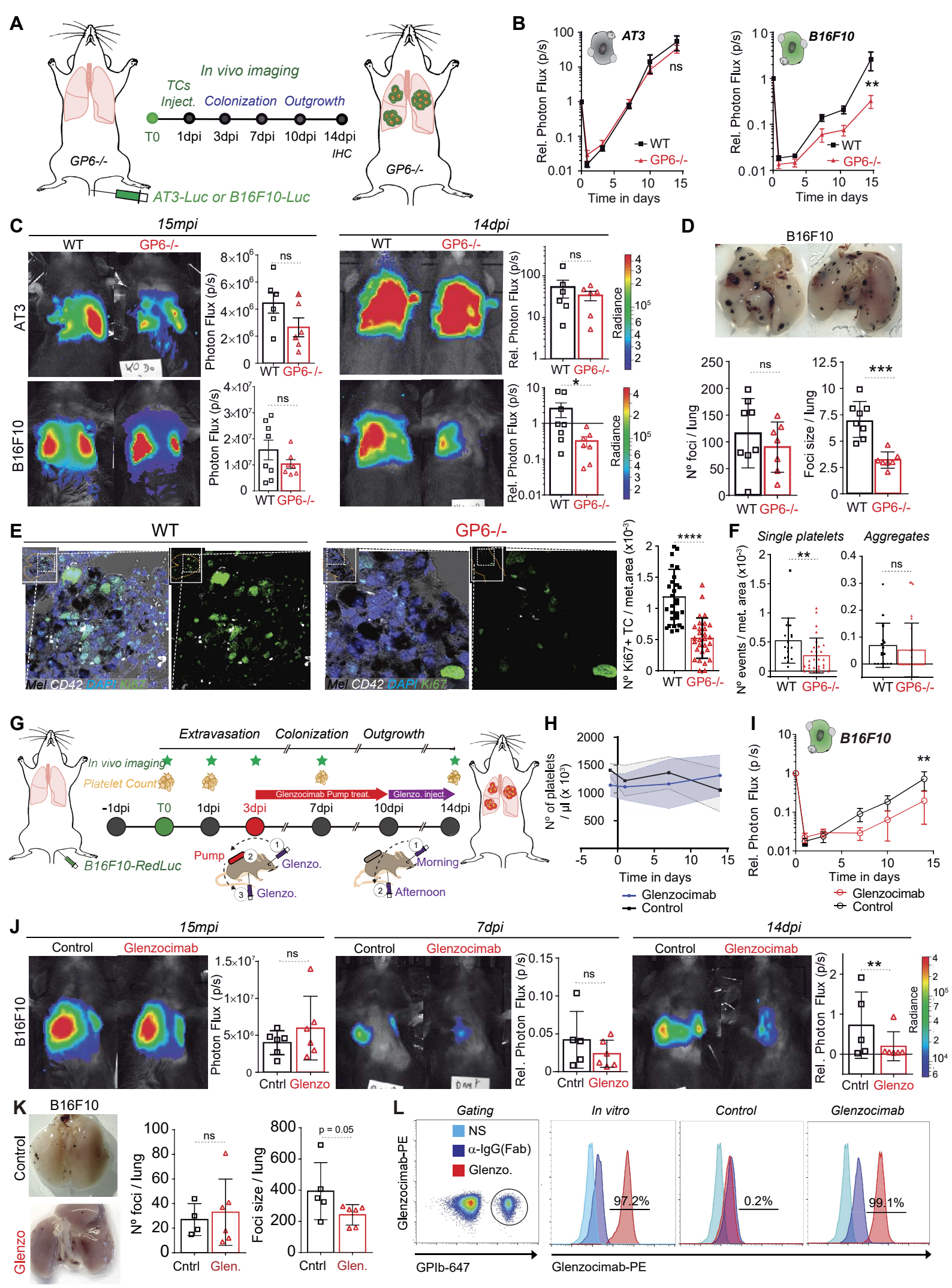

Figure 5. Garcia-Leon et al.

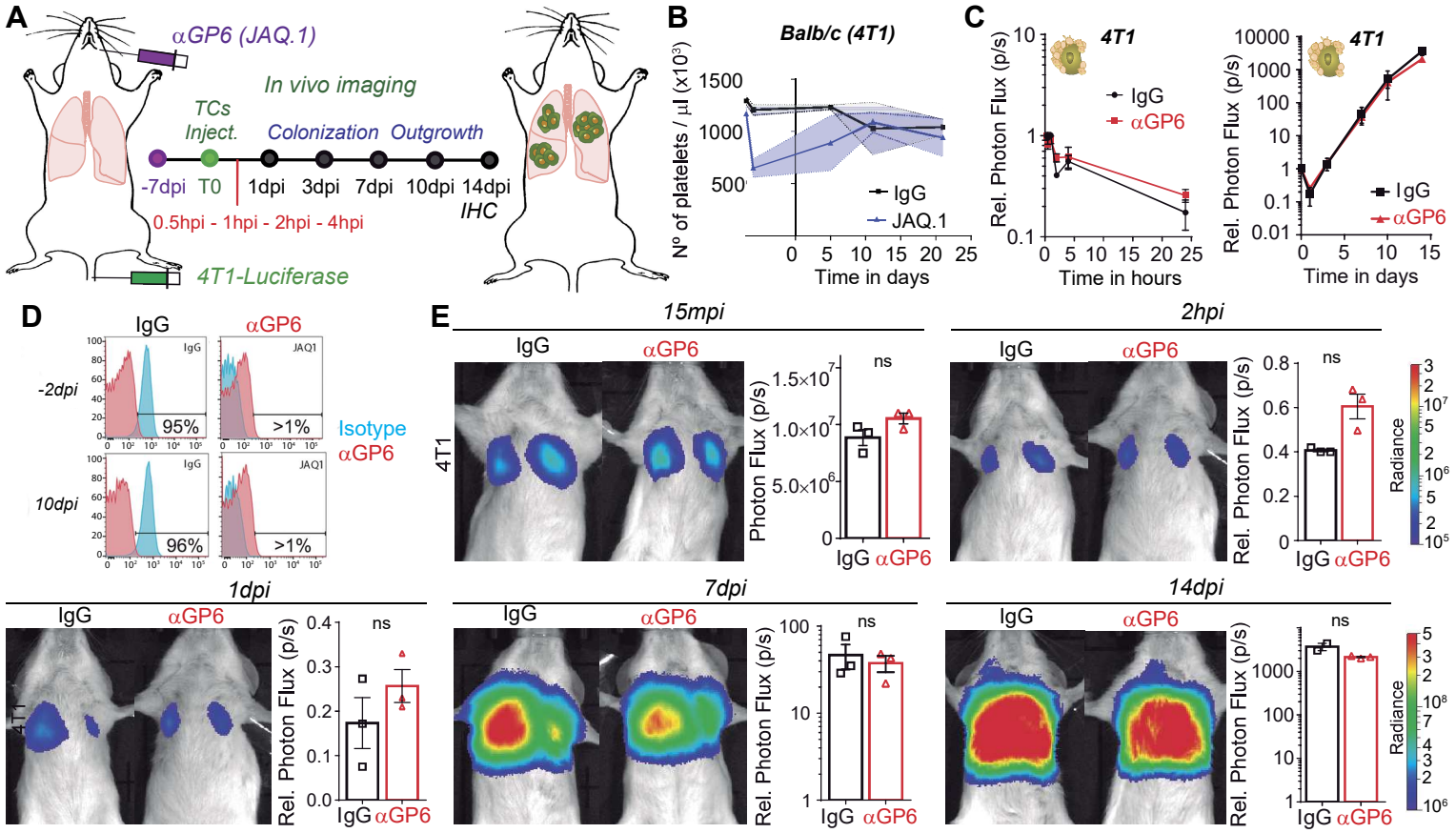

Supplementary Figure 6, related to Figure 5.
Garcia-Leon M.J. *et al.*